Joint inversion of surface wave dispersion and receiver functions: a Bayesian Monte-Carlo approach

Weisen Shen,[1] Michael H. Ritzwoller,[1] Vera Schulte-Pelkum[2] and Fan-Chi Lin[3]

[1]*Center for Imaging the Earth's Interior, Department of Physics, University of Colorado at Boulder, Boulder, CO* 80309, *USA.*
E-mail: Weisen.Shen@colorado.edu
[2]*Cooperative Institute for Research in Environmental Sciences and Department of Geological Sciences, University of Colorado at Boulder, Boulder, CO*
80309, *USA*
[3]*Seismological Laboratory, Division of Geological and Planetary Sciences, California Institute of Technology, Pasadena, CA* 91125, *USA*

SUMMARY

A non-linear Bayesian Monte-Carlo method is presented to estimate a Vsv model beneath stations by jointly interpreting Rayleigh wave dispersion and receiver functions and associated uncertainties. The method is designed for automated application to large arrays of broad-band seismometers. As a testbed for the method, 185 stations from the USArray Transportable Array are used in the Intermountain West, a region that is geologically diverse and structurally complex. Ambient noise and earthquake tomography are updated by applying eikonal and Helmholtz tomography, respectively, to construct Rayleigh wave dispersion maps from 8 to 80 s across the study region with attendant uncertainty estimates. A method referred to as 'harmonic stripping method' is described and applied as a basis for quality control and to generate backazimuth independent receiver functions for a horizontally layered, isotropic effective medium with uncertainty estimates for each station. A smooth parametrization between (as well as above and below) discontinuities at the base of the sediments and crust suffices to fit most features of both data types jointly across most of the study region. The effect of introducing receiver functions to surface wave dispersion data is quantified through improvements in the posterior marginal distribution of model variables. Assimilation of receiver functions quantitatively improves the accuracy of estimates of Moho depth, improves the determination of the Vsv contrast across Moho, and improves uppermost mantle structure because of the ability to relax *a priori* constraints. The method presented here is robust and can be applied systematically to construct a 3-D model of the crust and uppermost mantle across the large networks of seismometers that are developing globally, but also provides a framework for further refinements in the method.

Key words: Inverse theory; Surface waves and free oscillations; Seismic tomography; Crustal structure; North America.

1 INTRODUCTION

The construction of crustal and uppermost mantle velocity models over extended regions is critical to an understanding of continental tectonics and the thermal and compositional structure of the lithosphere as well as to provide the structural framework for an assessment of natural hazards. Surface waves provide spatially continuous information that is useful in developing 3-D shear wave velocity (V_s) models at regional (e.g. Levshin & Ritzwoller 1995; Ritzwoller *et al.* 1998; Levin *et al.* 2002; Ritzwoller *et al.* 2003; Levshin *et al.* 2005; Yang & Forsyth 2006; Shapiro *et al.* 2008; Yang *et al.* 2011), continental (e.g. Ritzwoller & Levshin 1998; Ritzwoller *et al.* 2001; Villasenor *et al.* 2001; Bensen *et al.* 2009) and global (e.g. Shapiro & Ritzwoller 2002; Ritzwoller *et al.* 2004)

scales. Receiver functions (RFs), in contrast, provide the spatially discrete local response of seismic waves to discontinuities beneath receiver locations (Vinnik 1977; Langston 1979). RFs also have been applied to construct local 1-D (Ammon & Zandt 1993) and 3-D models (Vinnik *et al.* 2004, 2006). The use of each type of data alone presents significant non-uniqueness problems (e.g. Ammon *et al.* 1990; Shapiro & Ritzwoller 2002): surface wave data do not image discontinuities whereas RFs do not strongly constrain absolute shear velocities between discontinuities (although they do constrain the contrast in *S*-wave velocity across the discontinuity). As a consequence, combining the two complementary data types was a natural direction for efforts to determine structure near to Earth's surface and was introduced more than a decade ago (e.g. Last *et al.* 1997; Ozalaybey *et al.* 1997), with numerous realizations of the idea

having subsequently been developed. Linearized joints inversions have been particularly popular (e.g. Du & Foulger 1999; Julia *et al.* 2000, 2003; Endrun *et al.* 2004; Horspool *et al.* 2006; Tkalčić *et al.* 2006; Gok *et al.* 2007; Pasyanos *et al.* 2007; Yoo *et al.* 2007; Tokam *et al.* 2010; Salah *et al.* 2011; Bailey *et al.* 2012).

Non-linear inversions based on model-space sampling methods such as Markov Chain Monte Carlo perhaps augmented by Bayesian approaches to construct ensembles of models that are used to quantify the degree of belief about earth structures (Mosegaard & Tarantola 1995; Sambridge 2001; Mosegaard & Sambridge 2002; Sambridge & Mosegaard 2002) also have been applied in both RF inversions (e.g. Shibutani *et al.* 1996; Zhao *et al.* 1996; Levin & Park 1997; Sambridge 1999a; Clitheroe *et al.* 2000; Piana Agostinetti *et al.* 2002; Bannister *et al.* 2003; Frederiksen *et al.* 2003; Nicholson *et al.* 2005; Vinnik *et al.* 2004, 2006; Lucente *et al.* 2005; Hetenyi & Bus 2007; Piana Agostinetti & Chiarabba 2008; Piana Agostinetti & Malinverno 2010) and surface wave inversions (e.g. Shapiro & Ritzwoller 2002; Yoshizawa & Kennett 2002; Socco & Boiero 2008; Maraschini & Foti 2010; Molnar *et al.* 2010; Khan *et al.* 2011) with varying degrees of theoretical sophistication, generality, spatial extent and data quantity. Joint inversions of RFs and surface wave dispersion or other geophysical data within the context of a non-linear, model-space sampling scheme are more rare and recent (An & Assumpção 2004; Chang *et al.* 2004; Lawrence & Wiens 2004; Vinnik *et al.* 2006; Liu *et al.* 2010; Moorkamp *et al.* 2010; Tokam *et al.* 2010; Basuyau & Tiberi 2011; Bodin *et al.* 2012).

Despite these advances, the joint interpretation of surface wave dispersion and RFs is still faced with at least four significant challenges. First, as traditionally applied, surface waves and RFs have yielded information at different lateral length scales. Secondly, also traditionally, surface wave dispersion information has derived from teleseismic earthquakes and has been produced mostly at long periods (>20 s), which are not ideally sensitive to the Earth's crust. Thirdly, joint quantitative interpretation requires meaningful uncertainties for both data types. Fourthly, the uncertainties in the resulting model must be quantified. Inextricably related to this is the need to find a model parametrization that possesses all and only the detail of structure necessary to fit both types of data. The purpose of this paper is to develop an approach to joint interpretation of surface wave dispersion and RFs that addresses these challenges in a practical, computationally efficient way that allows for automated application to large arrays of seismometers.

The first challenge has been ameliorated by the recent deployment of large seismic arrays such as the Earthscope/USarray Transportable Array (TA), CEArray in China (Zheng *et al.* 2010), the Virtual European Broadband Seismic Network and PASSCAL and Flexible Array experiments in which relatively close station spacing (50–100 km) allows much better resolution from surface waves. Recent developments in surface wave tomography have been stimulated to exploit these arrays. Examples of array-based surface wave tomography methods include the two-plane wave and related methods (Pollitz 2008; Yang *et al.* 2008a,b; Pollitz & Snoke 2010), eikonal tomography (Lin *et al.* 2009) and Helmholtz tomography (Lin & Ritzwoller 2011). These new array methods applied to data from the TA (e.g. Lin *et al.* 2011; Ritzwoller *et al.* 2011) and CEArray (Zhou *et al.* 2012) generate surface wave dispersion maps of unprecedented resolution (50–75 km) across large regions. In addition, tomographic methods based on ambient noise have been developed to augment information from teleseismic earthquakes. Ambient noise tomography (ANT) produces relatively short period (8–40 s) surface wave information that agrees with information

from teleseismic earthquakes in the period band of overlap (25–40 s; e.g. Yang & Ritzwoller 2008; Ritzwoller *et al.* 2011). Dispersion information from ambient noise, therefore, constrains the crust in a way that is directly complementary to RF analyses. The second challenge facing the joint interpretation of surface wave and RF information, therefore, is addressed by the development of ANT. Indeed, inversions for 3-D models of the crust and uppermost mantle based on surface wave dispersion information from ANT (perhaps with earthquake tomography) have been increasingly common in the past few years (e.g. Yang *et al.* 2008a,b, 2012; Bensen *et al.* 2009; Moschetti *et al.* 2010a,b; Lin *et al.* 2011; Zheng *et al.* 2011; Zhou *et al.* 2012).

The third challenge, determining uncertainty estimates for both types of data, has been partially solved recently for surface waves by the eikonal and Helmholtz tomography methods, which produce reliable error estimates for both ambient noise and earthquake tomography. We discuss in the Appendix a method to construct RFs referred to as harmonic stripping based on azimuthal harmonic analysis (e.g. Girardin & Farra 1998; Bianchi *et al.* 2010) that we use both to construct azimuthally independent RFs and estimate their uncertainty. Bodin *et al.* (2012) insightfully and in considerable detail discuss the importance of reliable uncertainty information, with particular emphasis on the need to estimate full data covariance matrices in the joint inversion. Finally, the fourth challenge, estimating model uncertainties, is addressed by the Bayesian Monte Carlo method that we develop and describe here. We show along the way that a quite simple model parametrization based on smooth B-splines in the crust and mantle can fit both data types at most locations across the western United States.

Therefore, we present here a non-linear Bayesian Monte-Carlo algorithm to estimate a V_s model beneath stations by jointly interpreting surface wave dispersion and RFs and associated uncertainties. The method is designed specifically to be applied automatically to large numbers of seismic stations. As a testbed for the method, we use 185 stations from the TA in the Intermountain West (Fig. 1). We first update the ambient noise and earthquake tomography to construct Rayleigh wave dispersion maps from 8 to 80 s across the study region. Eikonal and Helmholtz tomography are applied to
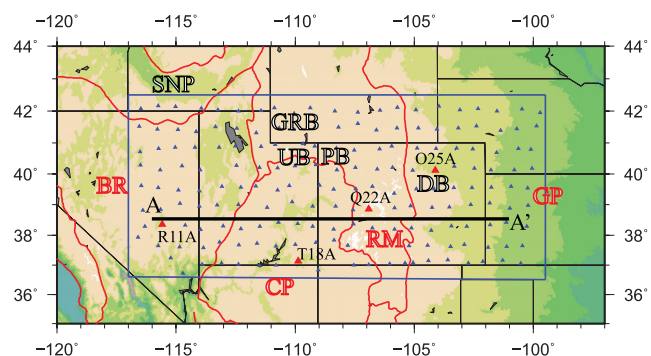

Figure 1. Stations of the Earthscope USArray Transportable Array (TA) used in this study are shown with blue triangles. The main geological provinces are outlined with red contours and titled with red abbreviations [the Basin and Range (BR) province, the Colorado Plateau (CP), the Rocky Mountains (RM) and the Great Plains (GP)]. Other regional geological features and basins are also identified with abbreviations [Snake River Plain (SNP), Green River Basin in Southern Wyoming (GRB), Uinta Basin in Northwestern Utah (UB), Piceance Basin in northwestern Colorado (PB) and Denver Basin in Colorado (DB)]. Four stations that are used to demonstrate the methods are identified with red triangles. The black line indicates transect A–A' ranging from the BR to the GP.

estimate uncertainties in ambient noise and earthquake dispersion information and the harmonic stripping method is used to generate backazimuth independent RFs with uncertainty estimates for each station. After applying the joint inversion (and for comparison the inversion based on surface wave dispersion alone) at each station, the final 3-D model of the crust and uppermost mantle is produced by interpolating between stations using simple-kriging at each model depth. Prior and posterior marginal distributions are presented to visualize changes in uncertainties for each data set. The study region is geologically diverse and structurally complex and provides an excellent proving ground for the methodology.

2 OVERVIEW OF THE METHOD

Monte Carlo and related parameter search algorithms (e.g. Sambridge 1999a) are designed to map data misfit across a broad range of model space. Within a Bayesian framework, these models are interpreted by computing the *a posteriori* (or posterior) probability distribution, which is the probability distribution of the model parameters given the observed data. Bayes' theorem allows the posterior distribution $\sigma(m)$ for a model m to be computed from the prior information on model space (given by the prior probability density $\rho(m)$ for model m) and the observed data as represented by the likelihood functional $L(m;$ the probability of observing the measured data given a particular model),

$$\sigma(m) \propto \rho(m)L(m). \tag{1}$$

Geophysical applications of Bayesian inference have been presented by Tarantola & Valette (1982), Mosegaard & Tarantola (1995) and Sambridge (1999b). The key steps are the expression of prior information as a probability density function and the computation of the likelihood functional, which is determined from data misfit. From a set of models distributed like the posterior distribution, one can then determine certain properties of the ensemble (e.g. best fitting model, mean model, median model), the covariance between model parameters, or the marginal distribution of particular model parameters or quantities derived from the model parameters.

The procedure we have developed to jointly invert surface wave dispersion information and RFs is similar in motivation and even is some of the details to the methods described by Bodin *et al.* (2011). We present a general overview of our methodology here as a guidepost to the principal results in the paper. We will also point out some differences with the method of Bodin *et al.* (2011). The data used in the inversion are described in detail in Section 3.

The model parametrization and the construction of the prior distribution are presented in Section 4. The prior information includes ranges in which individual model parameters are allowed to vary as well as rules that govern the relative values of different model parameters. Examples of the prior distribution for several model parameters are shown in Fig. 9.

The likelihood functional is simply related to the misfit function *S(m)* as follows:

$$L(m) = \exp\left(-\frac{1}{2}S(m)\right), \tag{2}$$

where

$$S(m) = \left(g(m) - D^{\mathrm{obs}}\right)^T C_e^{-1} \left[g(m) - D^{\mathrm{obs}}\right], \tag{3}$$

and D^{obs} is a vector of measured data, $g(m)$ is the vector of data predicted from model m, C_e is the data covariance matrix and T represents transpose of a vector. For surface wave dispersion here the vector D^{obs} consists of Rayleigh wave phase velocities observed

on a discrete set period grid and for RFs D^{obs} is the azimuthally independent RF over a fixed discrete time grid.

The Markov Chain Monte Carlo sampling of model space to generate the posterior distribution evolves as follows. A model m_j is selected from the prior distribution. A second model m_i is drawn and the likelihoods $L(m_i)$ and $L(m_j)$ are computed. The Metropolis law defines the probability of acceptance for model m_i,

$$P_{\mathrm{accept}} = \begin{cases} 1 & \text{if} \quad L(m_i) \geq L(m_j) \\ L(m_i)/L(m_j) & \text{if} \quad L(m_i) < L(m_j) \end{cases}. \tag{4}$$

That is, model m_i is accepted if its likelihood is greater than that of model m_j (i.e. its misfit is lower). Even if its likelihood is smaller than that of model m_j it may still be accepted, however. For example, if $P_{\mathrm{accept}} = 0.4$, we use a uniformly distributed random deviate generated between 0 and 1. If the value is less than 0.4 we accept the model. If the new model m_i is accepted, we define a new perturbation based on this model and search on. If the new model is not accepted, we make a record of it and its associated misfit information and start a new perturbation based on the previously accepted model m_j to choose the next step. The evolution of the algorithm in terms of improving misfit for surface wave data alone is shown in Fig. 8 and for the joint inversion in Fig. 11.

An additional model acceptance criterion then is applied to define the posterior distribution. In this we diverge from strict Bayesian methodology. If the data covariance matrix were known accurately, the choice of the acceptance criterion would be straightforward. Misfits to surface wave and RF data would be commensurable and the acceptance criterion would involve only choosing a probability threshold in the posterior distribution. As described later, because of difficulty in estimating the off-diagonal elements of the data covariance matrices, we have assumed that the surface wave dispersion data and the RFs have error processes that are independently but not identically distributed so that each covariance matrix is diagonal with elements σ_i^2 and s_j^2, respectively, for phase velocity at period i and RF at time j. This assumption has the practical effect that the misfits between the two data types are incommensurable. We are, therefore, forced to introduce a misfit scaling parameter κ to normalize the misfits between the two data types, as described in Section 6.1. The resulting joint misfit function, therefore, has the following form:

$$S_{\mathrm{joint}}(m) = S_{\mathrm{SW}} + \frac{1}{\kappa}S_{\mathrm{RF}} = \sum_{i=1}^{N} \frac{\left[g_i(m) - D_i^{\mathrm{obs}}\right]^2}{\sigma_i^2}$$
$$+ \frac{1}{\kappa}\sum_{j=1}^{M} \frac{\left[R_j(m) - A_0(t_j)\right]^2}{s_j^2}, \tag{5}$$

where $g_i(m)$ is the phase velocity predicted for model m at period i on a discrete grid of N periods, D^{obs} is the observed phase velocity, the function $A_0(t_j)$ is the observed RF at time t_j on a discrete grid of M times and $R_j(m)$ is the predicted RF for model m at time t_j. Somewhat different model acceptance criteria are applied in the inversion with surface wave data alone in Section 5 and in the joint inversion in Section 6. Example posterior marginal distributions are shown in Figs 9 and 12.

The methods that we present here differ from those of Bodin *et al.* (2011) in two principal ways. First, we choose smooth velocity profiles between specified boundaries at variable depths and fix the parametrization across the region of application. The nominal "transdimensionality" of the method of Bodin *et al.* refers to the variable parametrization of their method. We do not use an adaptive parametrization because, for the most part, we find that the

parametrization we choose is sufficiently flexible to fit the data. Secondly, as discussed above, we do not estimate the off-diagonal elements of the covariance matrices. Inspired by the hierarchical Bayesian formalism of Bodin *et al.* we attempted to estimate full covariance matrices for RFs, but found first that the estimated covariance matrices were singular and did not yield to matrix regularization methods designed to approximate the inverse matrices. Secondly, the covariance matrices that we derived were appropriate for a raw RF not the estimated azimuthally independent RF $A_0(t)$ that we use in the inversion. This is a subtle point that requires further analysis. For both reasons, we moved forward with diagonal covariance matrices for both dispersion data and RFs. Although these differences with the more general formulation of Bodin *et al.* (2011), which attempted to estimate the full covariance matrices for RFs, were motivated in part by our inability to estimate satisfactory covariance matrices, they do accelerate the inversion, which facilitates the application of the method to a large array like the US-Array. In addition, as we show, the method works well to improve 3-D models relative to those produced from surface wave dispersion data alone.

3 DATA PROCESSING

3.1 Rayleigh wave data processing

3.1.1 Ambient noise tomography (ANT)

The method of ANT is now well established, including cross-correlation of long pre-processed time-series to generate empirical Green's functions, measuring both Rayleigh and Love wave phase and group velocity curves and producing dispersion maps at particular periods (Shapiro *et al.* 2005; Yao *et al.* 2006; Moschetti *et al.* 2007; Yang *et al.* 2007). The data processing procedures that we adopt follow those of Bensen *et al.* (2007) and Lin *et al.* (2008), which we only briefly summarize here. First, raw vertical component seismograms recorded from 2005 to 2010 are downloaded from the IRIS DMC for the USArray TA stations in the western and central United States and are cut into 1-d time-series. The time-series length of each station is usually about 2 yr, but time-series lengths are variable and we do not apply a minimum time-series length restriction. Secondly, earthquake signals and other types of interference are removed by time domain normalization, in which the reciprocal of the mean of the absolute value of the waveform in a moving 80 s time window is used to weight the data point at the centre of the window. The weights are determined in the "earthquake band" between periods of 15 and 50 s period, but then are applied to the unfiltered data. Thirdly, the data are bandpass filtered between 5 and 100 s period and cross-correlation is performed between all station pairs. Then, Rayleigh wave group and phase velocity dispersion measurements are obtained from the symmetric component of each interstation cross-correlation by performing automatic frequency-time analysis (FTAN; Bensen *et al.* 2007). In this study, only Rayleigh wave phase velocity measurements are used. The automated FTAN dispersion measurements are winnowed by applying two criteria to select reliable measurements for surface wave tomography: (1) The interstation distance must be greater than three wavelengths at each period to ensure the far-field approximation and sufficient separation from pre-cursory noise and (2) signal-to-noise ratio (SNR) must be greater than 10 at each period for the measurement at that period to be accepted. Once all measurements are obtained, eikonal tomography (Lin *et al.* 2009) is

then applied to produce phase velocity maps from 8 to 40 s period. Eikonal tomography takes account of ray bending (off-great circle propagation) but does not model finite frequency effects (Lin & Ritzwoller 2011). One of the signature features of eikonal tomography is that it produces meaningful uncertainty estimates at each geographical location. This is done by accumulating phase velocity estimates at a given location from many central stations, fitting and then removing a truncated Fourier Series over azimuth to estimate azimuthal anisotropy, and then measuring the standard deviation of the mean of the residual. Figs 2(a)–(c) presents phase velocity maps from ANT at periods of 8, 20 and 36 s. By 40 s period, the SNR of ambient noise has decreased enough that high resolution phase velocity maps are no longer generated. Earthquake data are introduced to produce the longer period dispersion maps.

3.1.2 Earthquake tomography (ET)

The data processing procedure for teleseismic earthquake data is discussed by Lin & Ritzwoller (2011) and is only briefly summarized here. First, teleseismic records at the USArray TA stations in the western United States following earthquakes with surface wave magnitudes $M_s \geq 5.0$ are downloaded from the IRIS DMC and cut according to the arrival window of surface waves before instrument responses are removed. Secondly, FTAN is applied to the cut seismograms and Rayleigh wave front group and phase traveltimes and amplitudes are measured as a function of period. Phase ambiguity is resolved using a network-based approach in which traveltime measurements are compared with measurements at nearby stations using the method of Lin & Ritzwoller (2011). Then Helmholtz tomography is performed to produce Rayleigh wave phase velocity maps from 32 to 80 s period. Uncertainties are estimated similar to eikonal tomography applied to ambient noise data, but by accumulating phase velocities over many different earthquakes. In Helmholtz tomography, finite frequency effects are corrected through a term involving the local Laplacian of the amplitude field. Figs 2(d) and (e) shows the phase velocity maps from ET at periods of 36 and 70 s, respectively. A comparison of the 36 s phase velocity maps obtained from ANT and ET is shown in Fig. 2(f). The average difference is 5 m/s with slightly faster phase velocities emerging from ET.

3.1.3 Construction of phase velocity curves at station locations

After Rayleigh wave phase velocity maps are generated on a $0.2° \times 0.2°$ grid from both ANT and ET, phase velocity curves are interpolated to each station location. At short periods (8–36 s), phase velocity measurements and associated uncertainties are taken exclusively from ANT maps. At long periods (40–80 s) results are taken solely from ET maps. Between periods of 36 and 40 s, we weight the two velocity measurements by their local uncertainties and a smooth curve is produced. Fig. 3 shows four dispersion curves and uncertainty estimates for TA stations R11A, T18A, Q22A and O25A whose locations are shown on Fig. 1. In the overlapping period band, the phase velocity measurements from ANT and ET are overplotted, demonstrating the coherence between ANT measurements (red error-bars) and ET measurements (blue error-bars).

3.2 RF data processing

In the Appendix, we describe a method to estimate the azimuthally independent RF, $A_0(t)$, and associated uncertainty, *s(t)*, for each
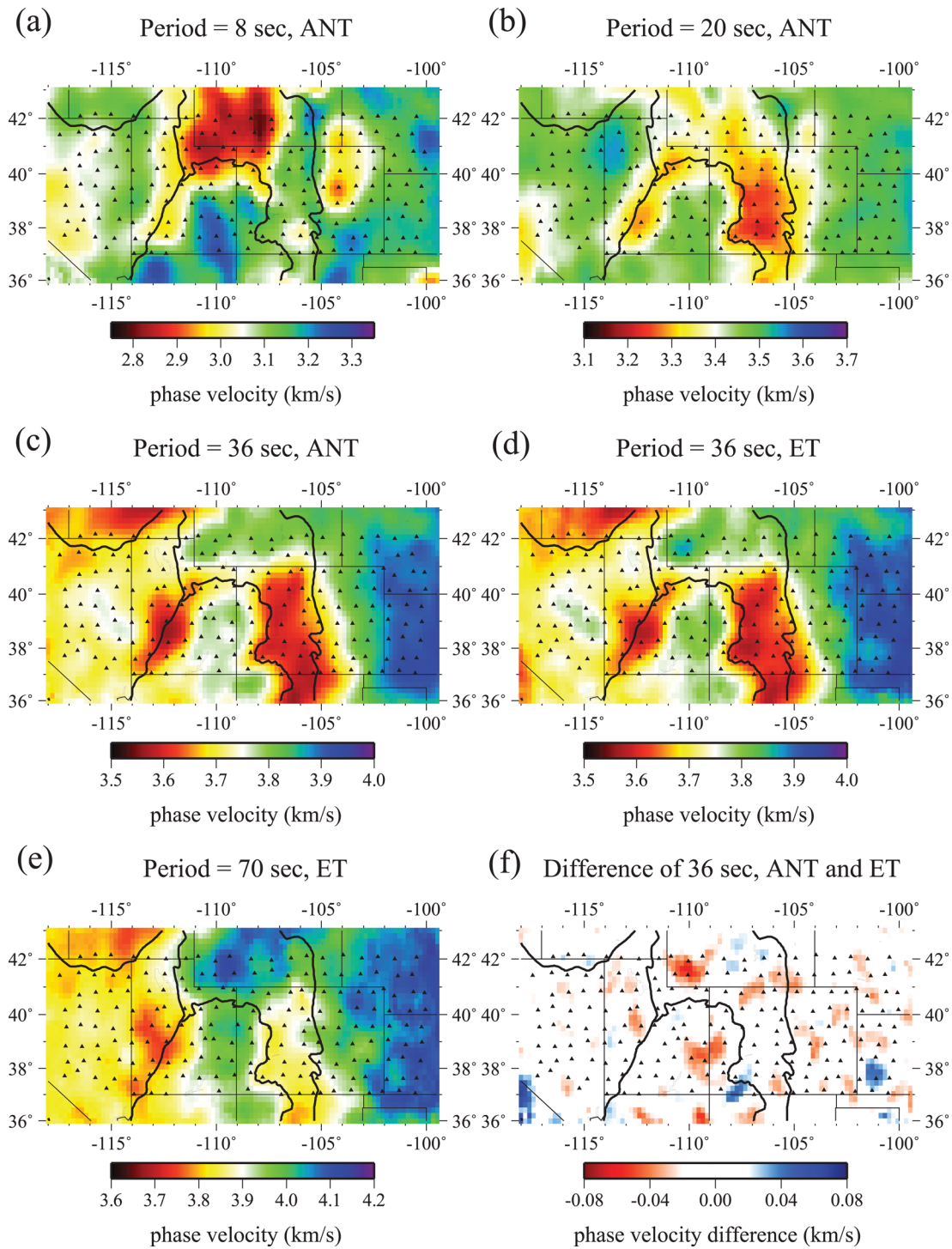
Figure 2. (a)–(c) Phase velocity maps at periods of 8, 20 and 36 s from ambient noise eikonal tomography (ANT). (d) and (e) Phase velocity maps at 36 and 70 s from earthquake Helmholtz tomography (ET). (f) Difference between the ANT and EQ results at 36 s period.

station. We refer to the method as 'harmonic stripping' because a truncated harmonic function is fit to the azimuthally dependent raw RFs for a given station at each time t,

$$H(\theta, t) = A_0(t) + A_1(t) \sin\left[\theta + \theta_1(t)\right]$$
$$+ A_2(t) \sin\left[2\theta + \theta_2(t)\right], \qquad (6)$$

where the A_i ($i = 0, 1, 2$) are the amplitudes of the three harmonic components and the θ_i are initial phases for the azimuthally

dependent components. This procedure approximately strips the azimuthal dependence from the RFs and produces the azimuthally independent RF, A_0. As shown in the Appendix, dipping crustal interface and azimuthal anisotropy dominantly produce signals with periodicities of 2π and π, respectively, which are largely removed via harmonic stripping so that the azimuthally independent component of the fit is a reliable estimate of the RF for a horizontally layered isotropic effective medium. Without complete and uniform azimuthal coverage, simply taking the average of the RFs over
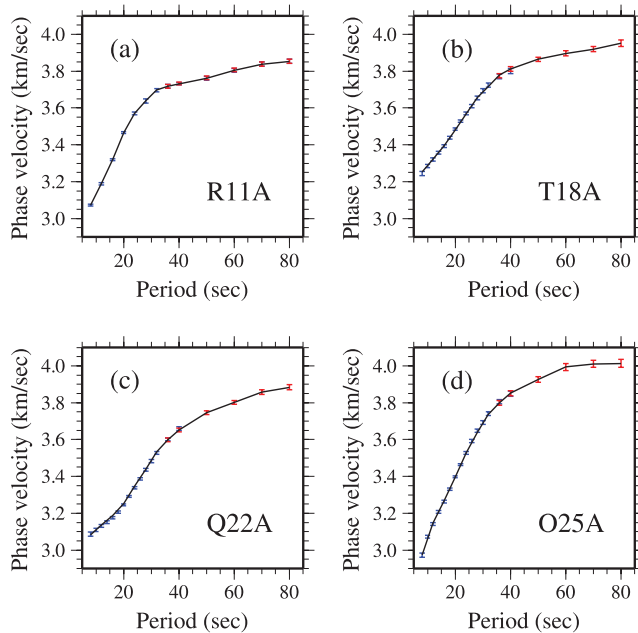
Figure 3. Phase velocity curves taken from the maps presented in Fig. 2 (and similar maps at the intervening periods) at the locations of stations R11A, T18A, Q22A and O25A, respectively. Blue symbols are uncertainties from the ambient noise tomography maps, red symbols are uncertainties for earthquake tomography maps and the line is the joint dispersion curve from the two kinds of measurements.

azimuth as is commonly done does not guarantee an unbiased estimate. The data processing and quality control (QC) procedures for the RFs are also discussed in the Appendix.

In this study we use Ps RFs (teleseismic *P*-to-*S* converted waves) exclusively, but Sp RFs could also be used in the context of the methods we develop, at least in principle (Vinnik *et al.* 2004). We select all teleseismic events in the NEIC PDE catalogue with a body wave magnitude $m_b \geq 5.1$ within the epicentral distance range of $30°$–$99°$ from each station. All sets of 3-component seismograms are rotated to form the radial and transverse components and are then bandpass filtered between 0.03 and 4 Hz using a Butterworth filter (2 poles, 2 passes). The harmonic stripping method and QC procedures have been applied to the 185 TA stations in the study region (Fig. 1). An example is shown in Fig. 4 for the TA station R11A. The QC'ed RFs presented over azimuth are shown in Fig. 4(a) and the harmonic function $H(\theta,t)$ fit to these RFs is shown in Fig. 4(b) for comparison. As described in the Appendix, the residual between these functions is used to define the uncertainty, $s(t)$, of the azimuthally independent RF and is presented in Fig. 4(c). The individual harmonic components are shown in Figs 4(d)–(f). The functions $A_1(t)$ and $A_2(t)$ quantify the azimuthally dependent signals that may be produced by tilts on internal interfaces and anisotropy, respectively. Some of these arrivals are observed to undergo a moveout at different azimuths. These functions could be applied to fine-tune the model presented here, but are not currently used for this purpose.

Several examples of the final azimuthally independent RFs $A_0(t)$ and associated uncertainties are shown in Fig. 5. The RFs display significant station-to-station variations. Those observed at station R11A in the Basin and Range province and station Q22A in the Rocky Mountains have strong *P*-to-*S* converted positive amplitude phases between 3 and 7 s delay time, suggesting a sharp rather than gradient transition from crustal to mantle velocities. The RF for TA

station T18A in the Colorado Plateau, in contrast, shows no Moho *P*-to-*S* conversion, which means that a gradient Moho is probable at this point. The RF for station O25A in the Great Plains has a strong negative arrival at ∼4 s caused by sedimentary layer reverberations at this location which probably interferes with observation of the Moho conversion.

4 MODEL PARAMETRIZATION AND DETERMINING THE PRIOR DISTRIBUTION

4.1 Model parametrization

Surface wave phase velocity curves and azimuthally averaged RFs are sensitive to the local average 1-D V_s structure beneath each location. For this reason, the inversion for a 3-D model reduces to a set of 1-D V_s inverse problems. We invert only for shear wave speed in the 200 km beneath the surface (reliable only to about 150 km) because the longest period of surface waves that we use here is 80 s. Below 200 km, the model is assumed to be constant. Because we use only Rayleigh waves, which are pre-dominantly sensitive to Vsv, we assume an isotropic Vsv model where $V_s =$ Vsh = Vsv. We set the V_p/V_s ratio to 2.0 in the sedimentary layer and 1.75 in the crystalline crust and mantle. The V_p/V_s ratio is important in RF analysis and it is discussed further in Section 8.1. For density we use the scaling relation (for 10 km) advocated by Christensen & Mooney (1995) in the crust and by Karato (1993) in the mantle. We apply a physical dispersion correction (Kanamori & Anderson 1977) using the Q model from PREM (Dziewonski & Anderson 1981), and the resulting model is reduced to 1 s period.

In a traditional surface wave inversion a 1-D model may be parametrized with smooth functions in the crust and mantle (Megnin & Romanowicz 2000), as a stack of layers (Yang & Forsyth 2006), or a combination of both (e.g. Shapiro & Ritzwoller 2002; Yang *et al.* 2008b; Moschetti *et al.* 2010). RF inversions are, however, typically parametrized with a set of fine layers (Cassidy 1992; Julia *et al.* 2000). We parametrize our model similar to some surface wave inversions in which B-splines represent structure in both the crystalline crust and the uppermost mantle as follows. (1) There is one sedimentary layer with a linear gradient velocity. Three parameters are used to describe this layer: layer thickness and Vsv at the top and bottom of the layer. (2) There is one crystalline crustal layer. Five parameters are used to describe this layer: layer thickness (km) and four B-spline coefficients for Vsv. (3) There is one uppermost mantle layer to a depth of 200 km. Five parameters are used to describe this layer: five B-spline coefficients for Vsv. The thickness of this layer is controlled by the thicknesses of the top two layers.

This model-parametrization contains 13 free parameters (Fig. 6). We explicitly seek vertically smooth models that fit the data. Here, smooth means that the model has no more vertical structure than required to fit the data within a specified tolerance and also that the model is continuous within some depth ranges. In this model parametrization, two discontinuities are introduced because the pre-dominant signals in RFs are from the Moho and, in the presence of sediments, from the sediment-basement contact. We demonstrate that a smooth parametrization can explain both the surface wave and RF data within data uncertainties across almost the entire study region. In other areas where a discrete higher-velocity lower crustal layer is observed (e.g. immediately north of our study area; Gorman *et al.* 2002), an additional crustal interface may be needed. The
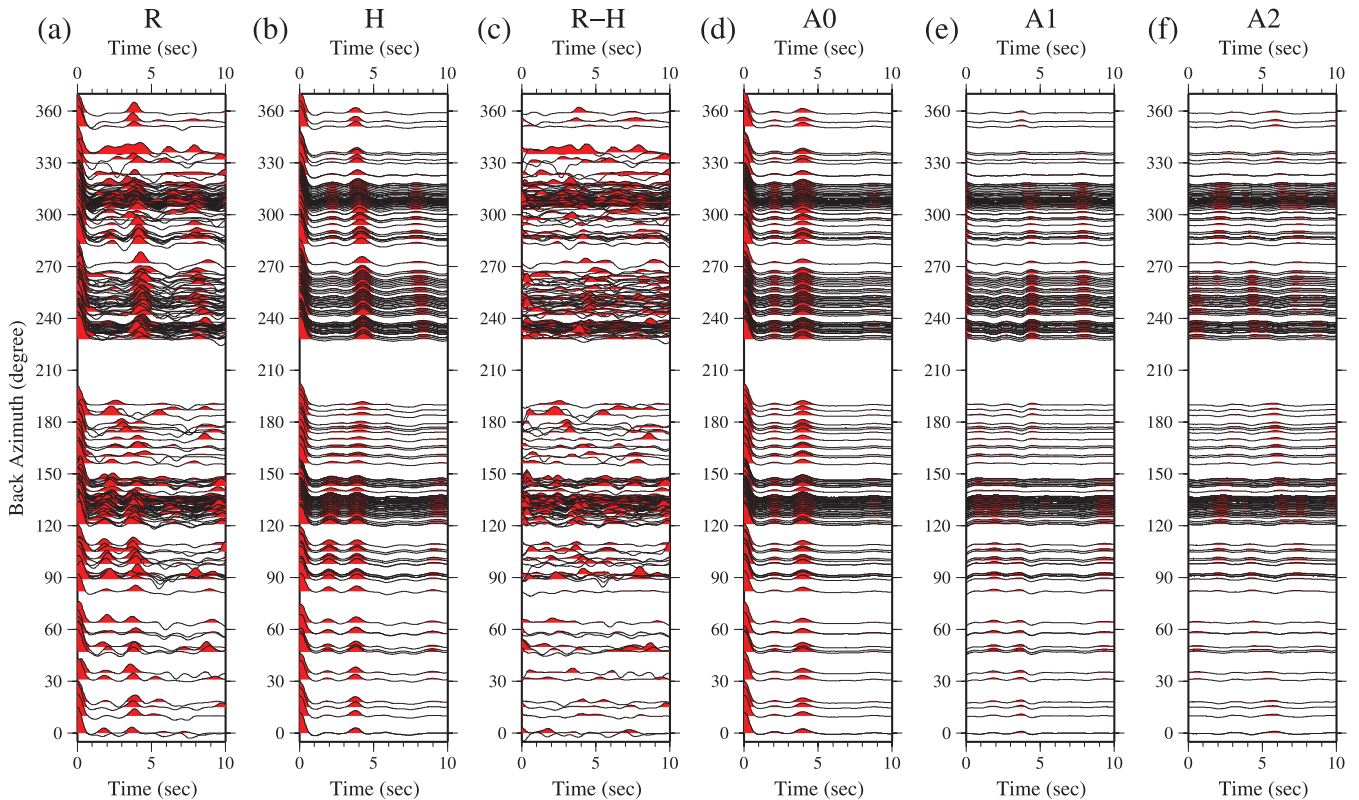
Figure 4. (a) The quality controlled receiver functions are plotted along backazimuth for station R11A. (b) The estimated receiver functions, $H(\theta,t)$, from harmonic stripping. (c) The difference between (a) and (b), from which uncertainties in the azimuthally independent receiver function are determined. (d)–(f) The three estimated components from harmonic stripping.

smoothness of the model is imposed by the parametrization so that ad hoc damping is not needed during the inversion.

With this model parametrization, we construct the model space in which the prior and posterior distributions are determined. The construction of the model space is based on perturbations to a reference model m_0, where sedimentary structure is taken from Mooney & Kaban (2010), crustal thickness from Bassin *et al.* (2000), and shear wave speeds in the crust and mantle from Shapiro & Ritzwoller (2002), as summarized in Table 1. At each location models are sampled around the reference in the range prescribed in the table. For example, the crystalline crustal thickness variation is ±25 per cent of the input value. If the reference thickness were 40 km, values would be considered from 30 to 50 km.

4.2 Determining the prior distribution

The prior distribution reflects the state of knowledge before data are introduced. Prior information that we apply in choosing models includes the following seven prior assumptions. (1) Models exist in the model space *M*, which is defined as the reference model subject to allowed perturbations (Table 1). (2) The model is continuous between Vsv discontinuities at the base of the sediments and Moho and is continuous in the mantle. (3) Velocity in the sedimentary layer increases with depth. (4) Velocity in the crystalline crust increases with depth (monotonicity constraint). (5) Velocity contrasts across the sedimentary basement and across the Moho discontinuity are positive. (6) $V_s < 4.9\,\text{km s}^{-1}$ throughout the model. (7) When surface wave data are used alone we apply the assumption of a positive velocity gradient in the uppermost mantle. Up to con-

straint (7), the prior distributions for inversions using only surface wave data or surface wave data jointly with RFs are identical. We discuss in Section 7.3 how constraint (7) may introduce bias in the estimated model, and how it can be eliminated when RFs are introduced. Together, these assumptions reduce model complexity and also ameliorate some of the velocity-depth trade-offs that occur in the surface wave inversion.

To determine the prior distribution, we perform a random walk in model space with the following steps. First, we initiate the model search at a random point in model space *M*. If this random point does not obey the assumptions listed above, it is rejected and another random point is chosen. Secondly, we introduce a random jump in model space. We simultaneously perturb all 13 parameters by selecting a new value randomly governed by a Gaussian probability distribution near the old value subject again to the previous assumptions. This Gaussian distribution is controlled by the width of the distribution (standard deviation), which is given in Table 2. These Gaussian widths have been chosen empirically to ensure the efficiency of the random walk in sampling the prior and posterior distributions. If the model produced is not contained in model space *M* (i.e. does not satisfy the seven constraints in the previous paragraph and does not fall within the ranges presented in Table 1), then the model is rejected and the process re-initiates.

With a sufficient number of sample points (>100,000), the prior distribution of each parameter can be viewed as histograms of marginal distributions of model characteristics at different depths such as those shown in Fig. 7 at the location of the TA station R11A. For this figure we generated Vsv models from such parameter distributions by converting the B-spline coefficients to Vsv values as a function of depth. Due to the lack of prior information imposed
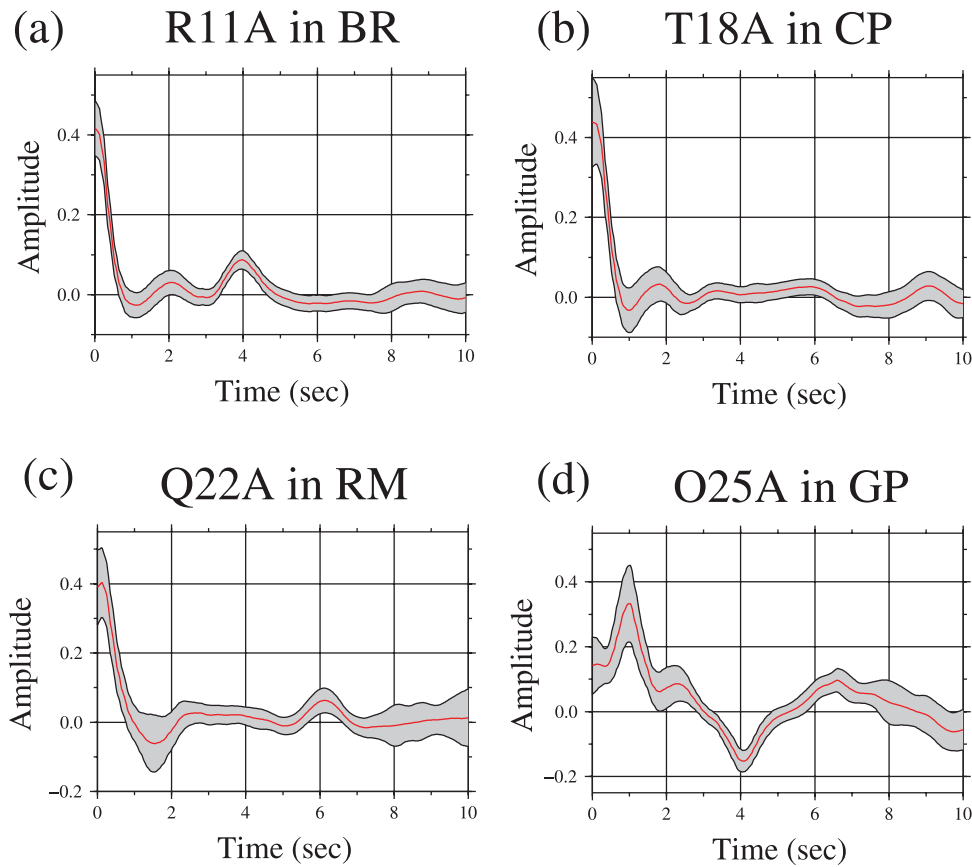
Figure 5. The estimated azimuthally independent receiver function ($A_0(t)$, red curve) and uncertainty ($s(t)$, grey corridor) for four stations whose locations are identified in Fig. 1. The uncertainty is the rms of the residual remaining after the harmonic fitting (eq. (A2)) to the azimuthally dependent receiver functions, reduced by a factor of two between 3 and 8 s.
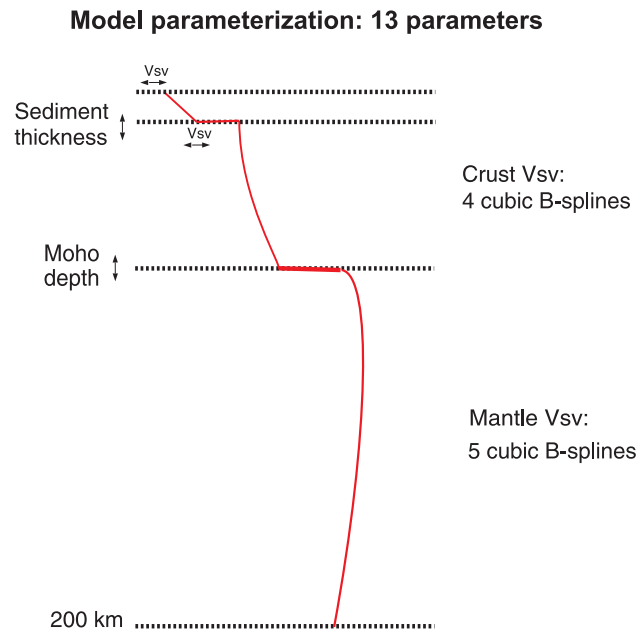

Figure 6. Model parametrization illustrating the 13 model parameters used in the Monte Carlo sampling of model space.

on the thickness of the sedimentary layer or on the thickness of the crystalline crust, the marginal prior distributions of both appear as uniform distributions (Figs 7a and c). However, the marginal distributions of V_s at different depths are not uniform because differ-

ent parameters interact through the prior assumptions. The resulting marginal distributions for these variables are more similar to tilted Gaussian patterns because they are affected by prior restrictions to sampling such as the monotonicity constraint on crustal velocities.

5 MONTE CARLO INVERSION OF SURFACE WAVE DISPERSION DATA

In this section, we discuss the Bayesian Monte Carlo inversion based on surface wave data alone for later comparison with the joint inversion with RFs, which is presented in Section 6. As above, we use the USArray TA station R11A in the Basin and Range province for examples and the input data for the inversion are shown in Fig. 3(a). At each location, Rayleigh wave phase velocities exist on a fixed discrete grid from 8 to 80 s period. Prior constraint (7) is not applied in this section.

5.1 The likelihood functional

For a problem in which the measurements are observed Rayleigh wave phase speeds at a particular location, which have independent but not identically distributed Gaussian observational uncertainties σ_i (period index i), the likelihood functional is computed from eq. (2) where the misfit function comes from the first term on the right hand side of eq. (5). The assumption of the frequency independence of error processes in surface wave dispersion is made here and in

Table 1. Model space and references.

Model parameters	Range	Reference
Sediment thickness	0–2 m_0 (km)	Mooney & Kaban (2010)
Crystalline crustal thickness	$m_0 \pm 0.25\, m_0$ (km s^{-1})	Bassin, C. *et al.* (2000)
Vsv, top of sedimentary layer	$m_0 \pm 0.2\, m_0$ (km s^{-1})	Bassin, C. *et al.* (2000)
Vsv, bottom of sedimentary layer	$m_0 \pm 0.2\, m_0$ (km s^{-1})	Bassin, C. *et al.* (2000)
B-spline coefficients, crust	$m_0 \pm 0.2\, m_0$ (km s^{-1})	Shapiro & Ritzwoller (2002)
B-spline coefficients, mantle	$m_0 \pm 0.2\, m_0$ (km s^{-1})	Shapiro & Ritzwoller (2002)

Table 2. Width of the Gaussian distribution in the model perturbation.

Parameters	Gaussian width
Thickness, sedimentary layer	0.1 km
Thickness, crystalline crust layer	1 km
B-spline coefficients, crust	0.05 km s^{-1}
B-spline coefficients, mantle	0.05 km s^{-1}
Velocity at top/bottom of sedimentary layer	0.05 km s^{-1}

other studies (Liu *et al.* 2010; Bodin *et al.* 2012), because the covariance over frequency is not well understood. The correlation of the dispersion velocities over frequency deserves further investigation.

5.2 Determining the posterior distribution

The information about model space extracted by introducing the data is described by the posterior distribution. As defined by eq. (1), the posterior distribution is the product of the prior distribution and the evaluation of fit to the observed data, which is summarized by the likelihood functional L. During model space sampling, when a new model m_i is generated by perturbing a given model m_j under the prior assumptions, the likelihood functional of this model is calculated through forward computation using the Thomson–Haskell method (computed using the code of Herrmann, http://www.eas.slu.edu/eqc/eqccps.html) with an earth-flattening transformation. Both of the likelihoods $L(m_i)$ and $L(m_j)$ are computed as discussed in Section 5.1, where the Metropolis law, eq. (4), defines the probability of acceptance for model m_i, as described in Section 2.

Fig. 8 shows an example of how the likelihood functional and misfit function of the models accepted during sampling of the posterior distribution evolve for TA station R11A. Accepted models are identified with circles, rejected models are not plotted. The trend shows that after about 100 samples, the likelihood functional will fluctuate near unity during the remaining iterations. We choose to stop iterating after 3000 sampling steps. To ensure that the starting point does not affect the sampling, we initiate the Monte Carlo sampling at ten different random models and the resulting statistics reflect these ten independent samplings. Fig. 8 also shows how the root mean square (RMS) misfit function, $\chi = \sqrt{N^{-1}S(m)}$, evolves. When $\chi < 1$, the fit lies within the estimated uncertainties, on average.

As discussed in Section 2, an additional model acceptance criterion is introduced as the basis for accepting models to form the posterior distribution. The minimum misfit χ_{min} is defined as the minimum value of χ found for all models visited during model space sampling. Once χ_{min} is found, we define the threshold of acceptance χ_{crit} for the surface wave inversion as follows:

$$\chi_{crit} = \begin{cases} 2\chi_{min} & \text{if} \quad \chi_{min} \geq 0.5 \\ \chi_{min} + 0.5 & \text{if} \quad \chi_{min} < 0.5 \end{cases}. \qquad (7)$$
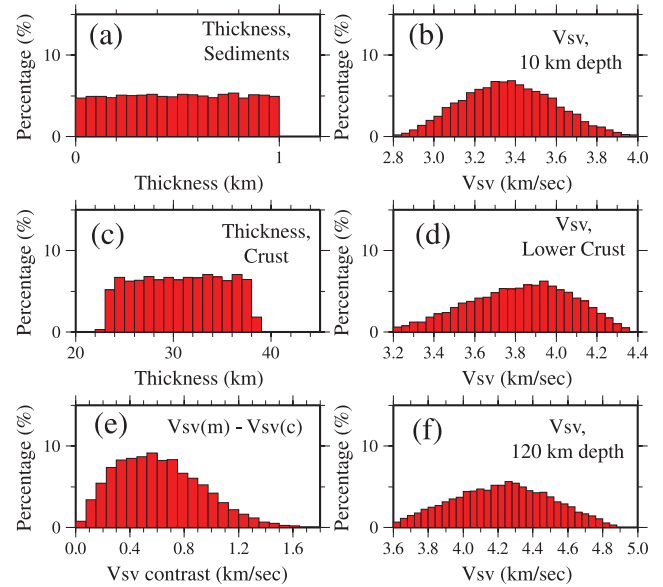

Figure 7. Prior distribution for several of the model parameters at the location of TA station R11A: Panel (a) sediment thickness, panel (b) Vsv at 10 km depth, panel (c) crustal thickness, panel (d) Vsv in the lower crust, panel (e) velocity contrast from 4 km above to 4 km below Moho (mantle–crust) and panel (f) Vsv at 120 km depth.
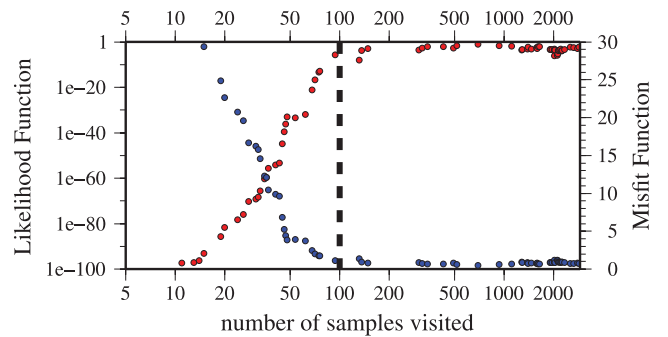

Figure 8. Convergence of the sampling of the posterior distribution of models when only surface wave dispersion data are used at the location of station R11A. Models are provisionally accepted according to the Metropolis Law in eq. (4), and then replaced by other models as the procedure evolves. Red dots are the likelihood function (eq. (2)) for each model that is accepted during the Metropolis sampling of model space, whereas blue dots are the rms-misfit (first term on the RHS of eq. (15)). The convergence point is at ~100 models (dashed line).

Thus, to define the ensemble of accepted models *a posteriori*, we accept any model m that is visited during the inversion as long as $\chi(m) \leq \chi_{crit}$. The choice of the critical threshold level below which models are accepted to form members of the posterior distribution is admittedly ad-hoc and deviates from strict Bayesian practice.
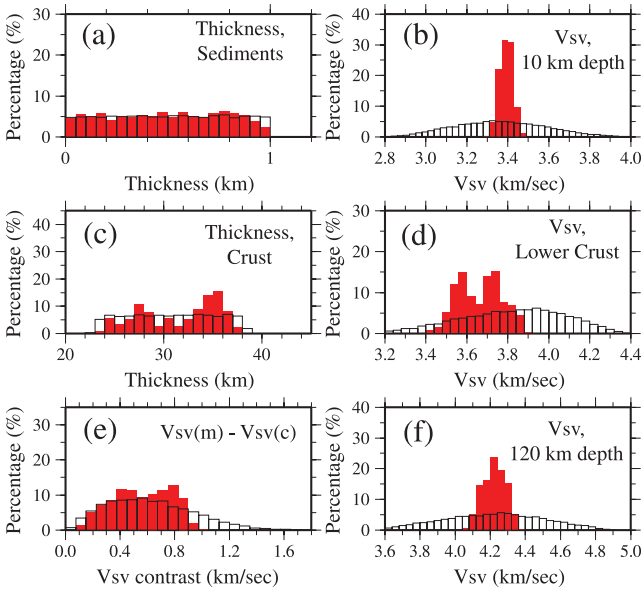
Figure 9. (a)–(f) The same as Fig. 7 for TA station R11A, but here the posterior distributions after Monte Carlo sampling using surface wave data alone (models fit the surface wave data) are plotted. The prior distributions from Fig. 7 are plotted as write histograms in the background. Surface wave data reduce the spread of structural velocities between boundaries, but have less effect on the depth to boundaries or velocity jumps across boundaries due to trade-offs between the parameters near the boundaries.

Eq. (7) succeeds to produce posterior distributions that capture our degree of belief in the final models, however.

From the set of accepted models in the posterior distribution, we compute the distribution of each parameter and the marginal distribution of Vsv at each depth. Fig. 9 presents example histograms of marginal distributions for several structural variables derived using surface wave data alone to compare with the prior marginal distributions shown in Fig. 7. Typically, the distributions of velocities between boundaries are narrowed. For example, Vsv at 10 km depth in the crust is narrowed; its standard deviation decreases by about a factor of six from ∼0.3 to ∼0.05 km s^{-1}. However, posterior distributions of discontinuity depths (Moho, sediments) or velocity jumps across the discontinuities do not decrease as appreciably. For example, crustal thickness and Vsv contrast across Moho are not changed strongly. These histograms demonstrate the sensitivity of Rayleigh wave dispersion to V_s structure. (1) Sedimentary thickness does not change because of the lack of very short period (<8 s) surface wave dispersion measurements. (2) Vsv at 10 km depth shows a much narrower distribution compared with the prior distribution because ambient noise provides information about this depth. (3) The mean of the crustal thickness distribution is about 33 km with a 1σ width of ∼3.6 km, showing that surface wave dispersion at this location possesses only weak sensitivity to the depth of the Moho discontinuity. The distribution is bimodal and not strongly peaked. (4) The marginal distributions of Vsv in the lower crust and the Vsv contrast across the Moho are narrowed somewhat but retain considerable uncertainties (0.15–0.2 km s^{-1}) and the lower crustal distribution is also bimodal. (5) Vsv in the uppermost mantle (120 km) is narrowed appreciably because the earthquake data are sensitive to this depth, but it is not constrained as well as at 10 km in the crust. This demonstrates that the vertical resolution of surface waves to local structure degrades with depth. Therefore, we only report structure to 150 km. These findings make intuitive sense and are quantified with the posterior distributions.

An alternative view of the results is provided by computing the mean, the median, the 1σ uncertainty and the full range of Vsv at each depth after all accepted models are identified. Fig. 10 shows the resulting extent of accepted models for station R11A. The grey corridors in Figs 10(a) and (b) outline the extent of all accepted models that fit the data, whereas the red lines present the 1σ width around the mean model. Note that without assimilating RFs, the crustal thickness (Moho depth referenced to the surface in Fig. 10b) is not well resolved and the predicted RFs (red waveforms in Fig. 10c) do not fit the observed azimuthally independent RF well, on average. There is also a strong trade-off between the lower crustal velocity and the uppermost mantle velocity. We show in Section 6 that these problems are ameliorated with the addition of RFs in the inversion.

6 MONTE CARLO INVERSION OF SURFACE WAVE DISPERSION AND RF DATA

When RFs are assimilated into the Monte Carlo algorithm, the prior distribution of models largely remains the same, although as we discuss in Section 7.3 we release the constraint on the positivity of the uppermost mantle velocity gradient. Here, we introduce the joint likelihood functional and then describe the posterior marginal distribution at TA station R11A and then for three other TA stations.

6.1 The joint likelihood functional

The joint likelihood functional is defined by eqs (2) and (5), but because we do not know the diagonal elements of the data covariance matrices we need to estimate the relative scaling of the misfits for surface waves and RFs that is quantified through parameter κ. We consider values of κ ranging from 1 to 40, and choose 2.5 as a value that strikes the appropriate balance between the two data sets. By choosing this value both data sets are approximately weighted equally in the inversion and the resulting misfits of the two data sets are comparable. The joint misfit function of eq. (5), therefore, becomes,

$$
\begin{aligned}
S_{\text{joint}}(m) &= S_{\text{SW}} + \frac{1}{2.5} S_{\text{RF}} = N\chi^2_{\text{SW}} + \frac{M}{2.5}\chi^2_{\text{RF}} \\
&= \sum_{i=1}^{N} \frac{\left[g_i(m) - D_i^{\text{obs}}\right]^2}{\sigma_i^2} \\
&\quad + \frac{1}{2.5} \sum_{j=1}^{M} \frac{\left[R_j(m) - A_0(t_j)\right]^2}{s_j^2},
\end{aligned} \tag{8}
$$

where we have implicitly defined the χ^2 misfit for surface waves and RFs. RMS misfit is the square root of χ^2.

6.2 Determining the posterior distribution in the joint inversion

Fig. 11 shows how the joint likelihood functional for station R11A evolves as model space is sampled. The convergence duration for this sampling is about 500 samples, which requires about five times more models than considered when surface wave data are used alone (Fig. 8). As with the surface wave inversion, we repeat the procedure starting from ten different random points to find the range of models that fit the data acceptably. The forward calculation of RFs is based on the code developed by Shibutani *et al.* (1996), which has also been used by Sambridge (1999a). We introduce
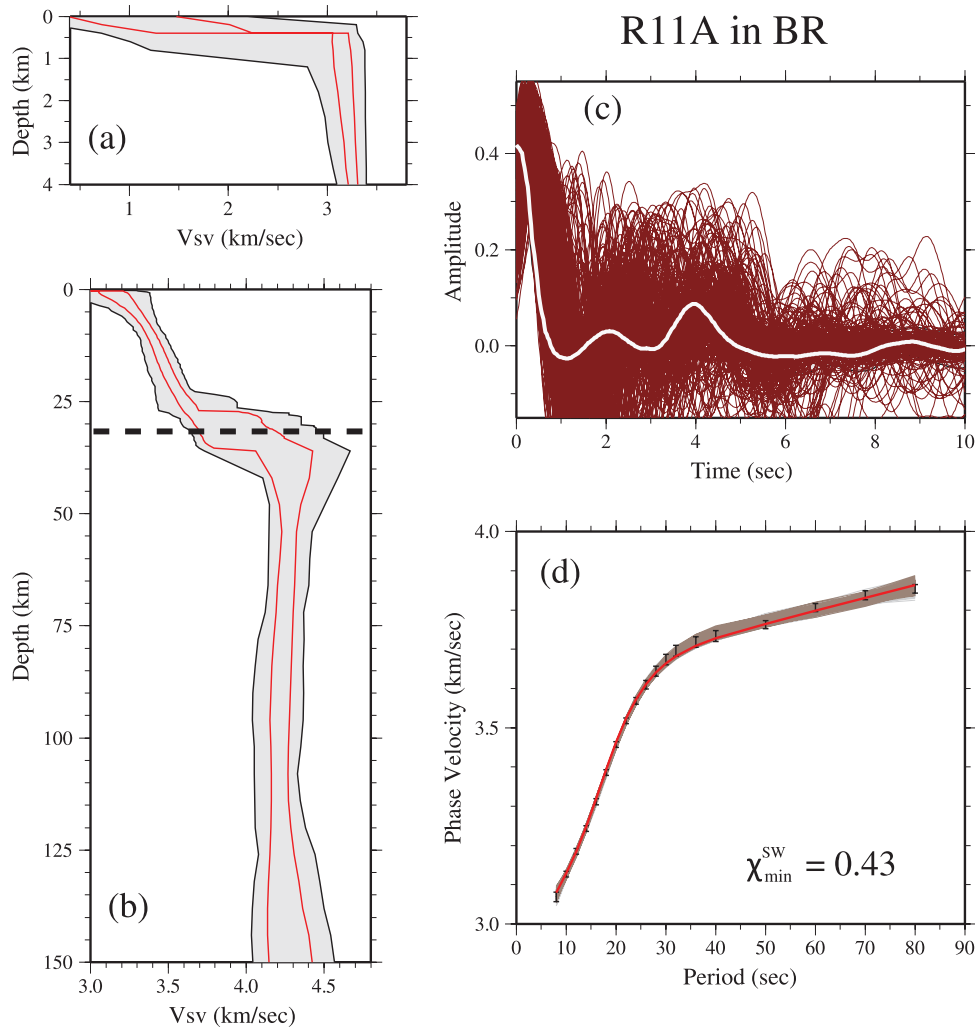
Figure 10. (a) and (b) The model ensemble at the location of TA station R11A in the Basin and Range province resulting from the Monte Carlo inversion of surface wave data alone is shown in full width (black lines with grey fill) and 1σ width (red corridor. Average Moho depth is identified as a dashed line at ~32 km. (c) The observed receiver function (white line) is plotted with predicted receiver functions (maroon lines) computed from all accepted models (eq. (7)), showing that receiver functions are not well fit, on average, by models constrained by surface wave data alone. (d) The observed Rayleigh wave phase velocity dispersion data (black error bars) are plotted with predicted surface wave phase velocity curves computed from all accepted models (eq. (7), grey lines). The red curve is the predicted phase velocity curve from the best fitting model.

for the joint inversion a somewhat different criterion than for the surface wave inversion as the basis for accepting models to form the posterior distribution. For each location, minimum RMS misfits for surface wave dispersion χ_{min}^{SW} and RFs χ_{min}^{RF} are identified, although the models that minimize misfits for these two types of data are generally not the same. The joint normalized relative RMS function χ^{joint} is defined as follows:

$$\chi^{joint} = \frac{1}{2}\left(\frac{\chi^{SW}}{\chi_{min}^{SW}} + \frac{\chi^{RF}}{\chi_{min}^{RF}}\right). \quad (9)$$

This function is a combination of relative RMS misfits for the two data sets. The criterion for model acceptance is $\chi^{joint} < \chi_{crit}$, where χ_{crit} is defined as,

$$\chi_{crit} = \chi_{min}^{joint} + 0.5. \quad (10)$$

For example, in the particular inversion for TA station R11A, the minimum misfit for the surface wave data is $\chi_{min}^{SW} = 0.51$, the minimum misfit for the RF data is $\chi_{min}^{RF} = 0.53$ and the minimum misfit to both data in the joint inversion is $\chi_{min}^{joint} = 1.15$. Thus,

the best fitting model that emerges from the joint inversion does not fit either data type optimally, but fits them both acceptably. In total, about 1000 models are found below the critical threshold $\chi_{crit} = 1.65$.

Example posterior marginal distributions are plotted and compared with prior (marginal) distributions in Fig. 12. All the marginal distributions change shape relative to the prior distributions, especially for Vsv at different depths and for crustal thickness. Compared with the posterior distributions using surface wave data alone (Fig. 9), the distributions of velocities in the crust and upper-mantle change only subtly (Figs 12b and f). The other distributions change profoundly. For example, crustal thickness at station R11A sharpens (from $\sigma = 3.6$ km to $\sigma = 1.3$ km). Concerning the velocity difference across the Moho, the mean increases and the standard deviation approximately halves. Such significant changes are expected because RFs are most sensitive to velocity contrasts across layer boundaries beneath the station; therefore, the position of the Moho is better determined as are the values of model variables that trade-off with Moho depth in the surface wave inversion.
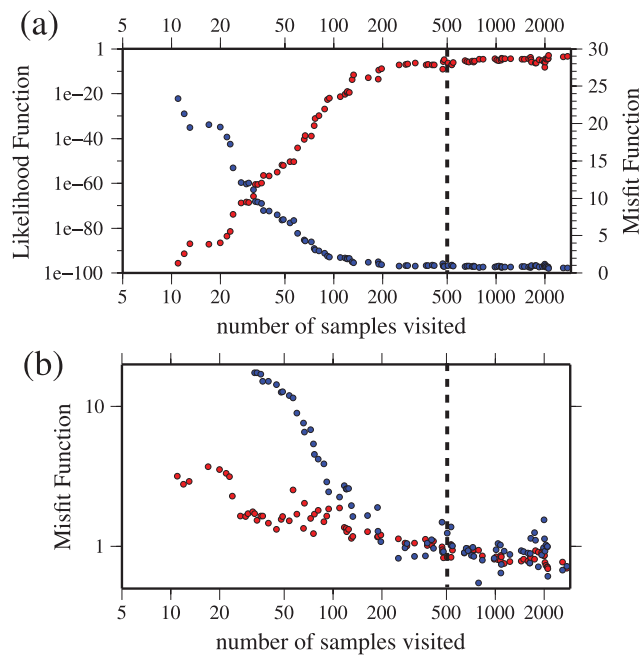
Figure 11. (a) The joint likelihood function (from eqs (2) and (8), red dots) and the joint misfit function (eq. (8), blue dots) for TA station R11A as a function of number of models sampled. (b) Misfit for each individual data set in the same search as (a). Blue dots are for surface wave phase velocity data and red dots are for the RF data. When the model converges to maximize the likelihood functional, both misfits typically converge to <1. In both plots, the location of 500 sampled models is identified with a dashed line, where the fit approaches convergence.

6.3 Examples of model ensembles

The model ensemble as well as the fit to the data at TA station R11A are shown in Fig. 13. The 1σ width is less than half of the full width of the model ensemble, because the Vsv distribution at any depth for the joint inversion is approximately Gaussian except for the sedimentary layer (see Fig. 12). Fig. 13(c) presents the azimuthally independent RF where the corridor outlined by black lines indicates the uncertainty range. The predicted RFs from the ensemble of accepted models are shown with grey lines and the model that fits the RF best is shown with the red line. The most prominent signal is the peak at about 4 s, which is fit quite well. However, the small trough near 2 s is not fit because doing so would require introducing another crustal discontinuity, which would violate monotonicity. The fact that the algorithm does not automatically adapt the parametrization to accommodate other discontinuities is discussed further in Section 8.2. Fig. 13(d) identifies the model that fits the surface wave data best, but the model that fits the RF best misfits the surface wave data somewhat between about 40 and 60 s period. The model that minimizes the joint misfit strikes a balance between these models.

Fig. 14 presents another example of the joint inversion for station T18A in the Colorado Plateau. In the observed RF, no clear peak is found from 3 to 8 s where the Moho *P*-to-*S* converted phase would be seen in "normal" RFs. After inversion, the RF data is well fit without a *P*-to-*S* converted arrival based on the model ensemble shown in Fig. 14(b). The Moho discontinuity is not well defined in the ensemble of models and Vsv changes smoothly from the lower crust to the uppermost mantle.

Fig. 15 summarizes the joint inversion result for station Q22A in the Colorado Rocky Mountains. In the observed RF, a peak at about 6 s suggests that the Moho is deeper than at station R11A in the Basin
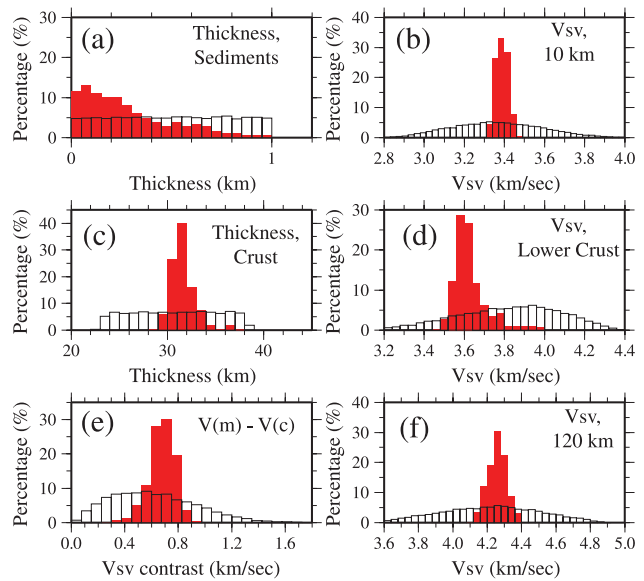

Figure 12. (a)–(f) The same as Fig. 9, but for the posterior distribution resulting from the joint inversion of surface wave phase velocities and receiver functions. Note the sharpening of distributions for parameters near the Moho in (c)–(e) compared to the distributions resulting from surface wave data alone (Fig. 9).

and Range province. As a result, the crustal thickness distribution is centred at about 49 km depth with an uncertainty of 2.3 km. The relatively small uncertainty of crustal thickness generates a sharp transition between the lower crust and uppermost mantle, particularly compared with station T18A in the Colorado Plateau.

Fig. 16 shows the joint inversion result for station O25A in a sedimentary basin, the Denver Basin region of the Great Plains. The peak at 1 s on the RF and the trough at 4 s indicate a thick sedimentary layer at shallow depths. After inversion, a thick sedimentary layer (~4 km) with a strong vertical velocity gradient is found and the crustal thickness is estimated to be 51.1 ± 3.9 km. Signatures in RFs that are common for sedimentary basins are a broadened direct *P*-pulse or an apparent lack of a direct *P*-arrival at zero delay time followed by a large amplitude arrival in the first second or so— the latter feature being due to bending to vertical incidence and a strong conversion to shear energy at the sediment-basement contact. The high-amplitude apparent mid-crustal negative arrival is modelled here as a reverberation within the sedimentary basin with two shear and one compressional legs within the sediment layer. The constraint of monotonically increasing velocities within the crust aids suppression of sediment multiples in favour of imaging true deeper crustal structure. In a few other locations in which there are true mid-crustal low-velocity layers, such as the Rocky Mountain location shown in Fig. 15, this may suppress a true feature, however. Extreme examples may be magma chambers (e.g. Wilson *et al*. 2003). Vsv in the sediments at O25A increases from less than $1 \, km \, s^{-1}$ to more than $3 \, km \, s^{-1}$ at depth of ~3 km, representing the compaction of sediments in this layer. Vsv in the upper crust is ~ $3.4 \, km \, s^{-1}$ and reaches higher than $4 \, km \, s^{-1}$ in the lower crust, perhaps indicating a mafic lower underplated crust ('7.× layer') that has been proposed for parts of the High Plains (e.g. Gorman *et al*. 2002). A fast lithosphere ($>4.5 \, km \, s^{-1}$) is observed in the upper mantle.
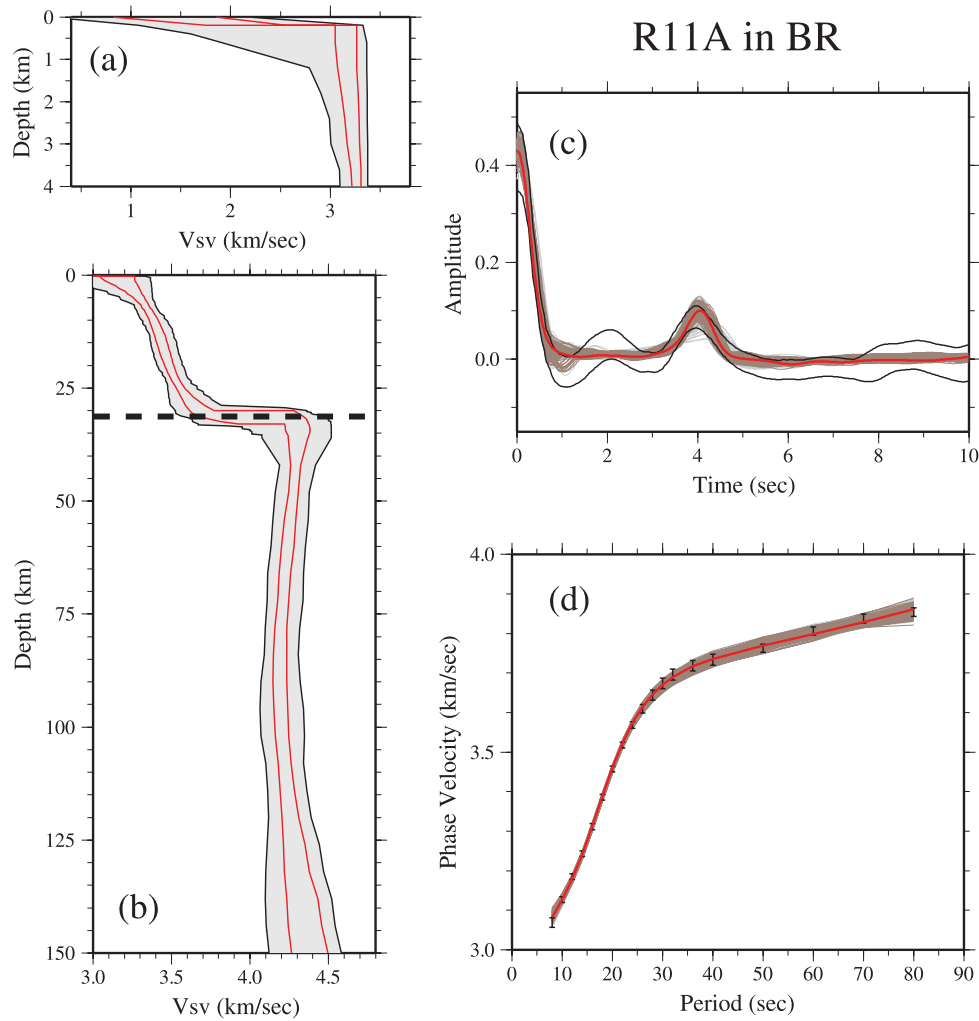
Figure 13. (a) and (b): The same as Fig. 10, but for results from the joint inversion of Rayleigh wave phase velocities and receiver functions at the same TA station (R11A). (c) The synthetic receiver functions from the accepted model ensemble are plotted with grey lines, with the best fitting receiver function shown as the red curve. The parallel black lines are the estimated uncertainty of the receiver function. There is a clear *P*-to-*S* conversion near 4 s period, necessitating a large velocity jump at a shallow Moho. (d) The predicted surface wave dispersion curves from all accepted models are plotted with grey lines with the best fitting curve identified in red.

7 SYSTEMATIC APPLICATION OF THE JOINT INVERSION ACROSS THE INTERMOUNTAIN WEST

In previous sections, the joint Bayesian Monte Carlo inversion of surface wave dispersion and RFs was shown to estimate reasonable 1-D models with attendant uncertainty information for stations situated in a wide variety of structural environments. We now report on the application of the joint inversion method to the 185 TA stations across the intermountain west (Fig. 1).

7.1 Construction of a 3-D Vsv model for the Intermountain West

We apply the Monte Carlo inversion to the 185 stations shown in Fig. 1. For each joint inversion, we identify the model from the resulting model ensemble that fits the surface wave data (SW) or RFs best as the SW or RF best fitting model, respectively. The misfits to SW data by the SW best fitting models for the stations tested are plotted with the white histogram in Fig. 17(a), whereas the misfits to the RFs by the RF best fitting models are plotted in Fig. 17(b).

For each station, the model with minimum joint misfit is identified, and is called the joint best fitting model. Misfits to SW and RF data from the joint best fitting models are shown in Fig. 17 with red histograms. At most stations, the joint best fitting models fit the SW or RF data only slightly worse than the model that fits each single data type best. This indicates that there is some tension in fitting the two data types. Secondly, the joint best fitting models have a misfit <1 for both data sets for almost all stations, which indicates that the simple model parametrization that we use in the joint inversion can reproduce the RFs with misfits below the RF uncertainties for most of the stations tested. Thirdly, larger RF misfits appear for stations near the corner of Utah/Colorado/Wyoming and are sparsely distributed through the Basin and Range. The RFs at those stations have sharp backazimuthal variations that vitiate the harmonic stripping method's attempt to estimate an azimuthally independent RF. Cases with sharp backazimuthal signals in the RFs are discussed further in the Appendix, but in these cases the uncertainty in the RF increases substantially and the inversion reverts for the most part to fitting surface wave data. Fewer than three stations show a large misfit (>0.9) to surface wave data and these stations are sparsely distributed across the map. Finally, the comparable minimum and
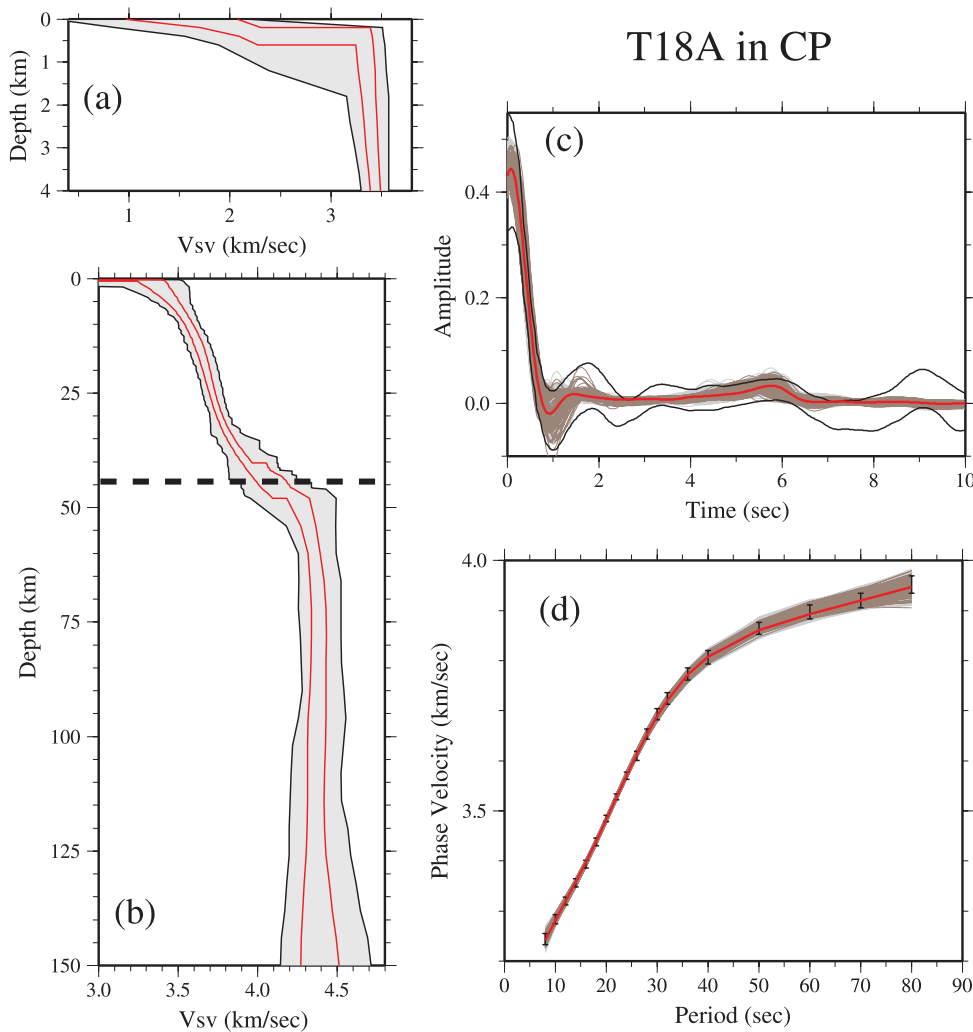
Figure 14. The same as Fig. 13, but for the result at TA station T18A located in the Colorado Plateau. No clear *P*-to-*S* Moho conversion is seen on the receiver function, probably implying a gradient Moho.

joint misfits for the two data sets also indicate that neither data set is overweighted during the inversion.

After inversion is performed at all stations, we obtain Vsv model ensembles beneath the 185 stations with means and uncertainties at all depths. The distribution of stations forms an irregular grid. To produce a smooth Vsv model on a regular grid, simple kriging (Schultz *et al.* 1999) interpolation is applied to smooth the Vsv values at each depth based on the mean value at that depth and the estimated uncertainties. For a given depth, at each grid node we search for stations within a 1-degree radius. We weight the average Vsv of the model ensemble for at given station using a weighting function defined as follows:

$$W_i = \begin{cases} \dfrac{1}{(1+d_i)\sigma_i} & \text{if } d_i \leq 1^\circ \\ 0 & \text{otherwise} \end{cases}, \qquad (11)$$

where d_i and σ_i denote the distance to station i from the grid node and the uncertainty of the model at the specified depth for that station, respectively. By performing this simple-kriging interpolation, map views of the 3-D model on a $0.25^\circ \times 0.25^\circ$ spatial grid are produced.

7.2 Characteristics of the 3-D model

In the upper crust (10 km depth, Fig. 18a), high velocities are observed beneath the Colorado Plateau and Great Plains, whereas the Rocky Mountains show low Vsv. Near the northern boundary of the Colorado Plateau low velocities are also observed, presumably caused by very thick sediments in the Green River Basin, Uinta Basin, etc. At these locations, the maximum allowed sediment thickness may be less than the true thickness, leading to smearing of low velocities into the upper portion of the crystalline crustal layer. In contrast, the Denver Basin is much thinner than 10 km and the structure there is well constrained by RF data. Uncertainties at 10 km depth are approximately homogeneous across the region, averaging about 27 m s^{-1}, which is about 0.8 per cent.

In the lower crust (averaged from 4 km above the Moho to the Moho, Fig. 18c), the most prominent feature is the slow anomaly (<3.6 km s^{-1}) encompassing the eastern Basin and Range province near the northwestern Colorado Plateau. Slow lower crust is found across the entire Basin and Range and also near the western edge of the Rocky Mountain province in southwestern Colorado. There is coincidence between the $\sim$3.85 km s^{-1} Vsv contour and the eastern Rocky Mountain topographic high in Colorado, implying a strong relationship between topography and crustal structure.
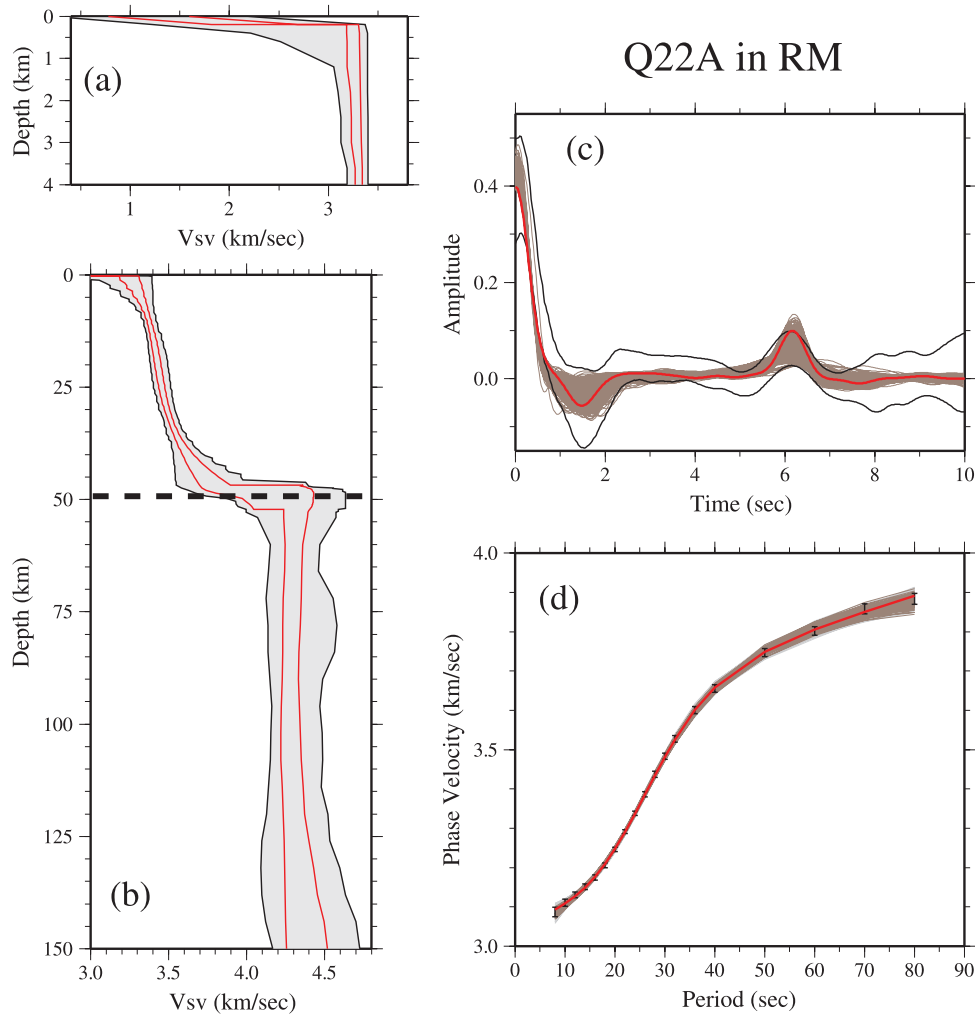
Figure 15. The same as Fig. 13, but for the result at TA station Q22A located in the Colorado Rocky Mountains. A clear *P*-to-*S* conversion is seen near 6 s, requiring a large velocity jump at a deeper Moho than in Fig. 13.

A fast lower crustal anomaly extends through the Colorado Great Plains and southern Wyoming and also penetrates into the Colorado Plateau. Uncertainties are larger and more variable in the lower crust (Fig. 18d) than the upper crust, ranging from about 40 m/s in parts of the Colorado Plateau to more than 160 m s^{-} in the Rocky Mountains of southern Colorado. Higher uncertainties have two causes. First, they appear where there is a large jump in velocities across the Moho, due to a trade-off between Moho depth and uppermost mantle structure. The trade-off has been ameliorated but not entirely eliminated through the addition of RFs in the inversion. Secondly, larger uncertainties also occur where RFs have a larger uncertainty in the amplitude of *P*-to-*S* conversions.

At 60 km depth (Fig. 18e), which is in the uppermost mantle across the region, a strong contrast is observed between the eastern and western sides of the study region. A strong anomaly as low as 4.0–4.1 km s^{-1} is seen at the eastern edge of the Basin and Range, which may be related to the Cenozoic magmatism in this region (Roy *et al.* 2009). Much higher velocities are observed beneath the Great Plains, reaching up to 4.8 km s^{-1}. Uncertainties are largely homogeneous across the study region, averaging about 50 m s^{-1} (Fig. 18f). At a depth of 120 km (Fig. 18g), Vsv beneath the Great Plains is very high, but the strongest high velocity anomaly is detected beneath the Wyoming Craton in southern Wyoming. This high velocity feature continues beneath the Colorado Plateau, suggesting

a strong, thick lithosphere beneath the northern Colorado Plateau except for its northwestern periphery. The Basin and Range and Rocky Mountains show relatively homogeneous low Vsv compared with other regions. Uncertainties (Fig. 18h) are fairly homogeneous and average about 65 m s^{-1} (<1.5 per cent) across the entire study region. Uncertainties are larger deeper in the mantle (120 km versus 60 km) because the surface wave dispersion information is less sensitive to deeper structure.

7.3 Changes in the 3-D model compared with the surface wave inversion

There are several significant advantages to adding RFs to surface wave dispersion data in the Monte Carlo inversion. We focus on three topics: (1) determining crustal thickness and uncertainties, (2) determining the velocity jump across the Moho and (3) constraining uppermost mantle structure.

By utilizing RFs in the inversion, there is a natural increase in the accuracy of estimates of Moho depth or crustal thickness. This is apparent on comparison between the crustal thickness distribution for station R11A from the inversion with surface wave data alone and that from the joint inversion of both data sets (Figs 9c and 12c). This observation holds for all stations with clear *P*-to-*S* converted
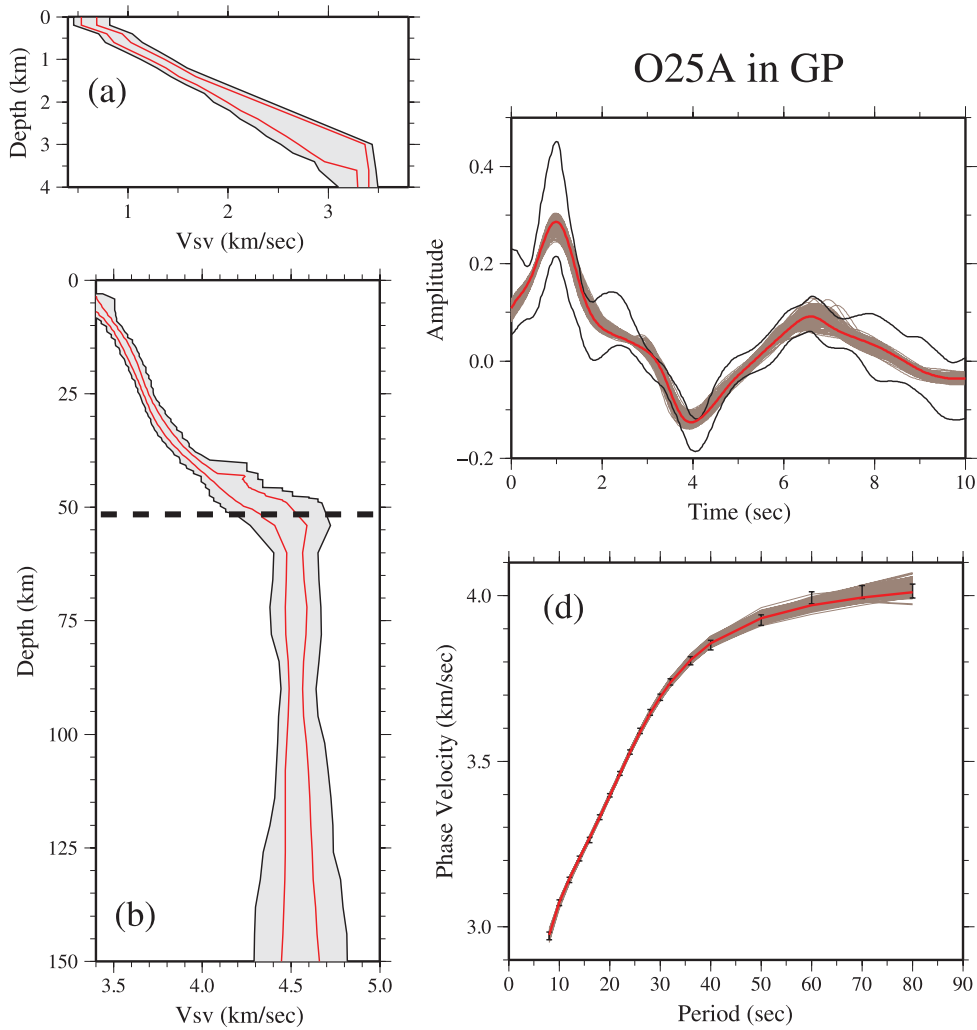
Figure 16. The same as Fig. 13, but for the result at TA station O25A located in the Great Plains. Strong sedimentary reverberations dominate the receiver function adding uncertainty in the location of and velocity jump at the Moho.
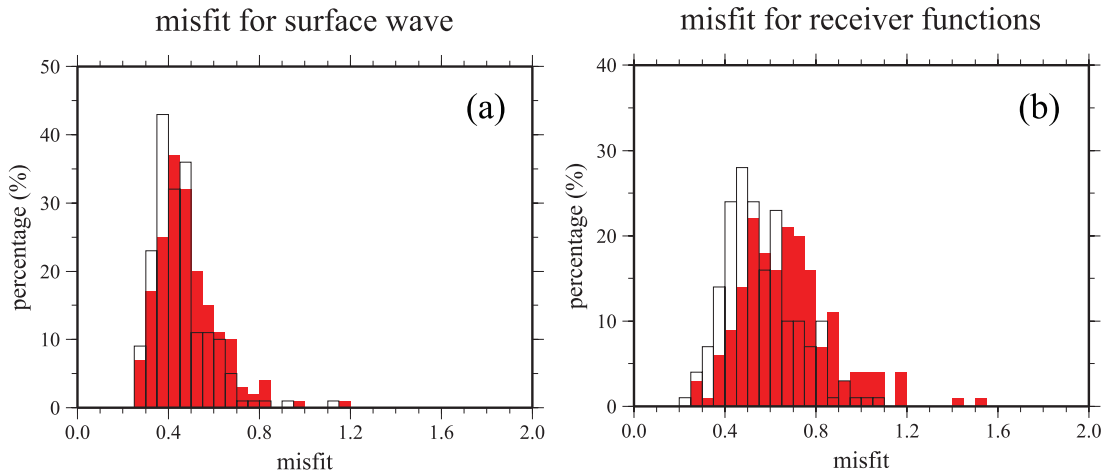

Figure 17. (a) Misfit histogram showing the misfits to surface wave data over the spatial grid covering the area of study. The white histogram is for the model that best fits the surface wave data at each point and the red histogram is for the model that jointly best fits both surface wave and receiver function data. At most gridpoints, the jointly best fitting models fit the surface wave data only slightly worse than the model that fits the surface wave data best. (b) Same as (a), but for receiver functions. The white histogram is for the model that best fits the receiver function data at each location and the red histogram is for the model that jointly best fits both data sets. At most gridpoints, the jointly best fitting models fit the receiver function data only slightly worse than the model that fits the receiver function data best.
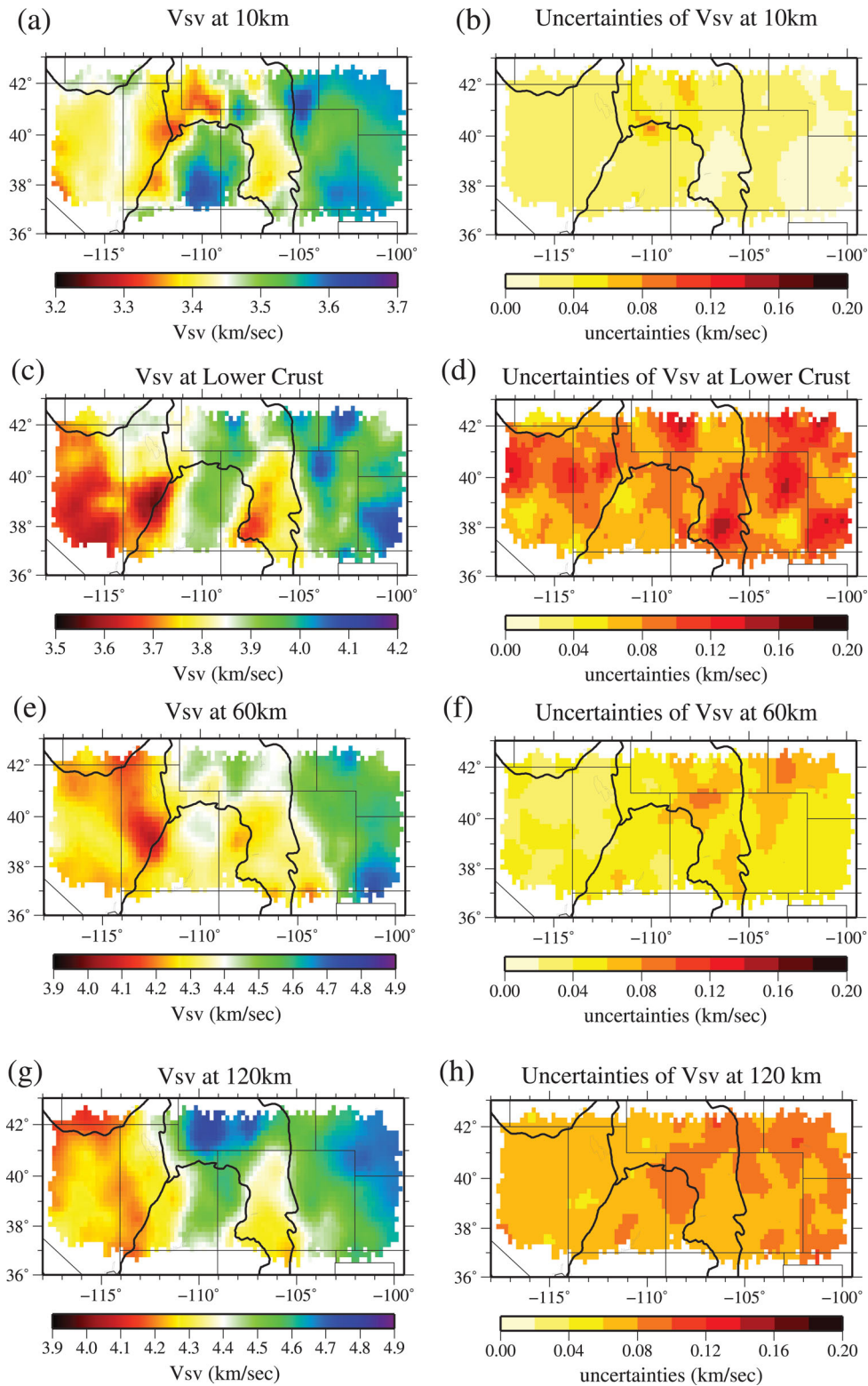
Figure 18. Map views of Vsv at different depths (left) with uncertainties (right). (a) and (b) Vsv at 10 km depth. (c) and (d) Vsv in the lower crust, 4 km above Moho. (e) and (f) Vsv at 60 km depth. (g) and (h) Vsv at 120 km depth.

signals. Figs 19(a) and (b) presents crustal thickness and associated uncertainties from inverting surface wave dispersion data alone. The uncertainty level scales with crustal thickness and is ∼5 km on average with smaller values in the Basin and Range and larger values in the Great Plains. In contrast, crustal thickness and un-

certainty determined from the joint inversion appears in Figs 19(c) and (d). The uncertainty level from the joint inversion decreases in the Basin and Range, the central Rocky Mountains and parts of the Great Plains, where *P*-to-*S* converted phases are well observed. In the northern part of the Colorado Plateau and southern Wyoming
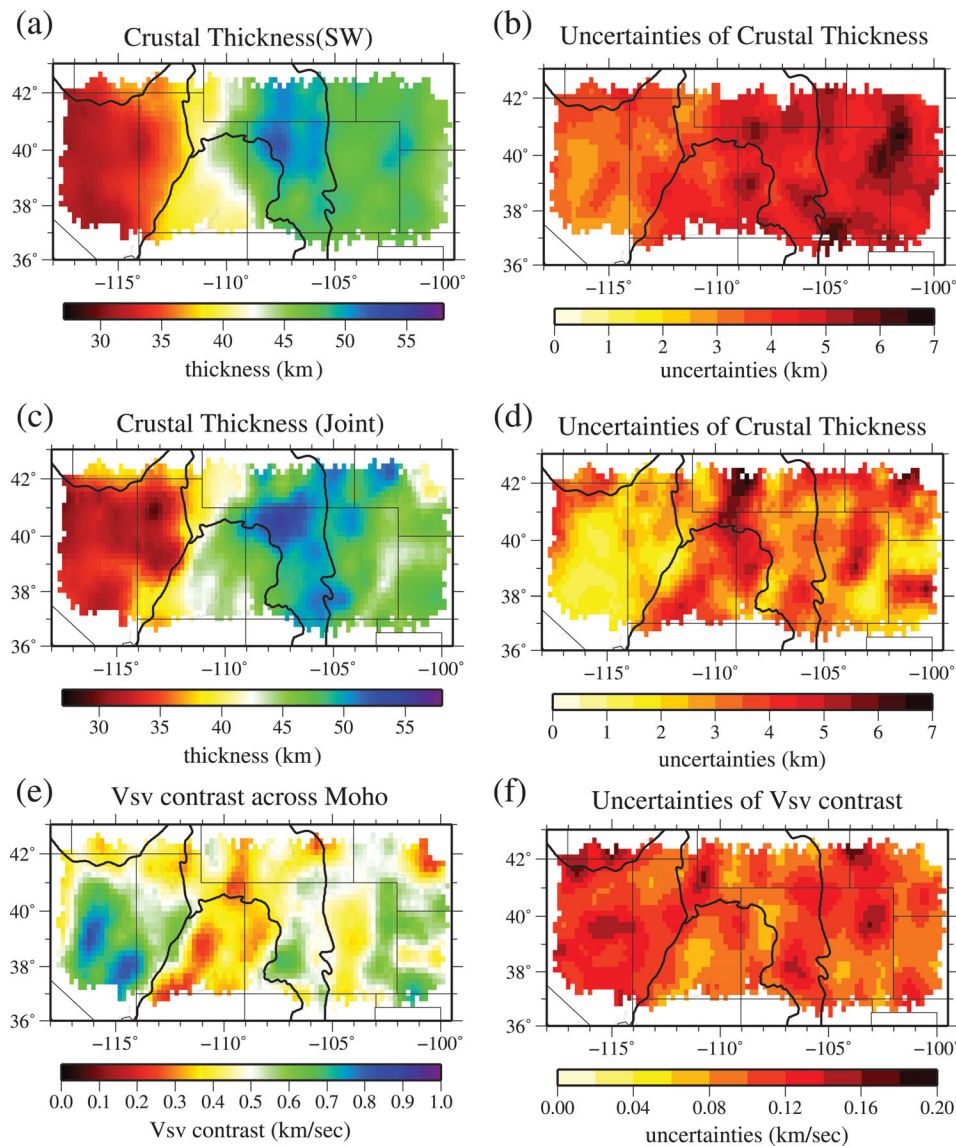
Figure 19. (a) and (b) Crustal thickness and its uncertainty resulting from inversion of surface wave data alone. (c) and (d) Crustal thickness and its uncertainty resulting from the joint inversion of surface wave and receiver function data. (e) and (f) Vsv contrast from 4 km below to 4 km above Moho and its uncertainty from the joint inversion of surface wave and receiver function data.

craton where thick sediments exist, crustal thickness uncertainties are not reduced by adding RFs or may even increase where the *P*-to-*S* signals in the RFs are muted by sedimentary reverberations. In addition to improving the determination of Moho depth, RFs also help to determine whether a sharp Moho discontinuity exists or not. An example is shown in the inversion at station T18A in the Colorado Plateau (Fig. 14), where the raw RF has no dominant arrival from 3 to 7 s where a *P*-to-*S* conversion should appear. The joint Monte Carlo inversion thus produces a model that has a gradient in Vsv at the depth where Moho is expected. The resulting crustal thickness distribution has larger uncertainty than when a clear *P*-to-*S* phase is observed, but none of the models in the distribution shows a sharp Moho.

Secondly, introducing RFs improves the determination of the Vsv contrast across the Moho, which is related to the amplitude of the *P*-to-*S* phase in the RFs. For instance, the RF at station R11A (Fig. 13) shows a strong Moho conversion whereas the converted phase in the RF at T18A is weak, resulting in a Vsv contrast at Moho that

is stronger at R11A than at T18A (or perhaps a gradational crust–mantle transition at station T18A). A map of the Vsv contrast and uncertainty across the region is shown in Figs 19(e) and (f). The features shown are coherent with geological province. A high Vsv contrast across Moho is observed beneath the Basin and Range as well as parts of the Rocky Mountains and the Great Plains east of the Denver Basin. In contrast, beneath the Colorado Plateau, especially under the northwestern Colorado Plateau, the Vsv contrast is very low. This feature is consistent with observations made by earlier studies (Sheehan *et al.* 1997; Gilbert & Sheehan 2004; Levander *et al.* 2011; Bailey *et al.* 2012). Beneath the southern Wyoming Craton, we observe a small Moho Vsv contrast as well as high uncertainties in crustal thickness and thick sediments. This is because sedimentary reverberations dominate the RF where a Moho peak would be expected and the Vsv constrast across Moho is difficult to resolve. Uncertainties in the velocity contrast across Moho range between about 80 to 160 m s^{-1}, being smallest in the Colorado Plateau where the Vsv contrast is low in all accepted models.
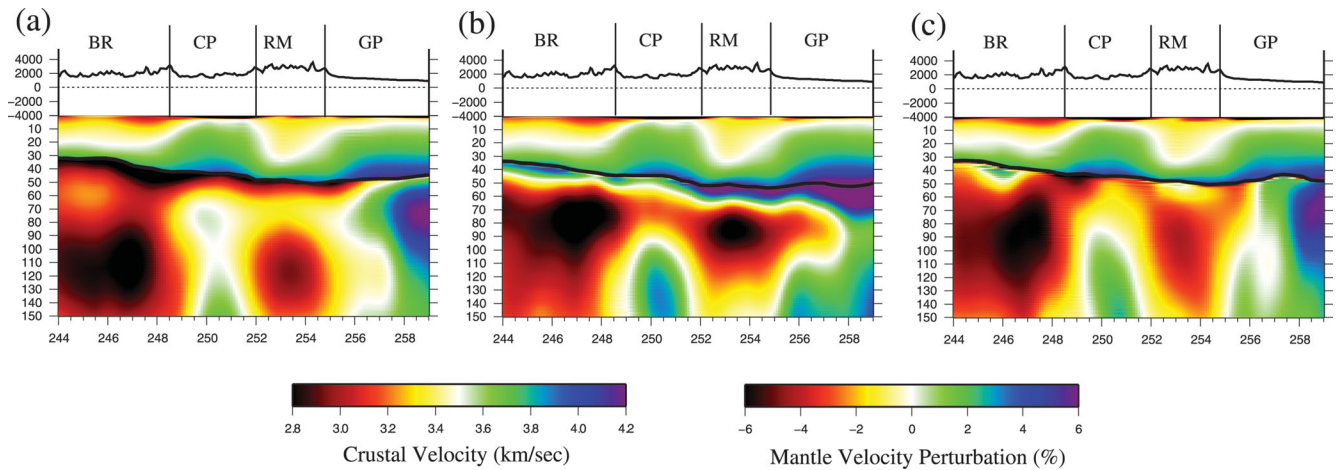
Figure 20. (a) Vsv model along transect AA' in Fig. 1 constructed using surface wave data alone with a positive gradient constraint in the uppermost mantle. (b) The same as (a), but with a negative constraint on the uppermost mantle velocity gradient. (c) Vsv model from the joint inversion of both surface wave and receiver function data with no constraint on the Vsv gradient in the uppermost mantle. Crustal structure is presented in absolute shear wave speed but mantle structure is presented as the percent perturbation relative to $4.4\,\mathrm{km\,s^{-1}}$. Geological provinces are presented with abbreviations (Fig. 1) overlying surface topography.

The third advantage of the joint inversion method is a better determination of mantle structure below the Moho discontinuity. This is largely due to reduction of the trade-off between Moho depth and lower crustal velocity. Because of this trade-off, when surface wave dispersion is used alone to invert for a 3-D model, a prior constraint is often applied on the vertical velocity gradient in the uppermost mantle. For example, several studies have set the Vsv gradient in the uppermost mantle to be positive (Yang *et al.* 2008b; Moschetti *et al.* 2010; Zheng *et al.* 2011). Fig. 20 shows the result of various upper-mantle constraints along the transect identified in Fig. 1. In the model constructed by using surface wave data alone with an imposed positive Vsv gradient in the uppermost mantle (Fig. 20a), a slow anomaly belt is found immediately beneath the Moho. In contrast, if the constraint is changed in sign so that a negative Vsv gradient is imposed, a fast anomaly belt is observed (Fig. 20b). These two models show differences down to depths of more than 100 km and the placement of anomalies in depth is affected strongly. Lithospheric thickness and the depth to prominent asthenospheric anomalies are both changed by varying this constraint. However, both models fit the surface wave data equally well, which indicates that the surface wave data alone cannot distinguish between them. Fig. 20(c) shows the model constructed from the joint inversion of surface wave dispersion and RF data with no constraint on the uppermost mantle velocity gradient. The result looks like a combination of Figs 20(a) and (b). Beneath the Basin and Range where the Moho is prominent and the Vsv contrast across Moho is large, the model is more similar to Fig. 20(b) constructed with a negative gradient constraint in the uppermost mantle. However, in places where a gradient Moho is expected, the model is more similar to models from the positive gradient constraint, Fig. 20(a). The assimilation of RFs in the inversion resolves the velocity-depth trade-off with data rather than with ad hoc prior constraints.

8 DISCUSSION

8.1 Sensitivity to the V_p/V_s ratio

Rayleigh wave phase velocity dispersion curves are only weakly sensitive to V_p compared to V_s; hence, the V_p/V_s ratio is usually a fixed parameter in the inversion of surface wave data. However, the V_p/V_s ratio is important in RF analysis because it is needed to map the *P*-to-*S* conversion time delay to depth. The V_p/V_s ratio can be determined when Moho reverberations such as the PpPs or PsPs phases are used as discussed by Zhu & Kanamori (2000). However, these phases arrive later than the 10 s time window used here in the Monte Carlo inversion. We omit these phases from consideration because at many locations in the western US Moho reverberations cannot be isolated cleanly due to lateral heterogeneity (e.g. the large scatter in the results of Lowry & Perez-Gussinye 2011, Fig. 2a) and in some places a graditional crust–mantle transition. Rayleigh wave ellipticity and local amplification may also potentially be used to constrain the crustal V_p/V_s ratio (Lin *et al.* 2012a,b). However, this is beyond of the scope of this study.

Because we ignore crustal reverberation phases, we are unable to determine the three relevant parameters (V_s in the crust, crustal thickness and V_p/V_s ratio) simultaneously. To demonstrate this result, we add an extra degree of freedom to the model space, the V_p/V_s ratio in the crystalline crust, which we allow to vary between 1.65 and 1.85 during the inversion. First, the posterior distribution of the V_p/V_s ratio as well as its prior distribution are plotted in Fig. 21(a). The posterior distribution of the V_p/V_s ratio does not centre at any particular value. Secondly, once the V_p/V_s ratio is introduced as a variable in the inversion, the posterior distribution of the crustal thickness broadens (Fig. 21b) about 20 per cent compared with the same posterior distribution from the inversion with fixed V_p/V_s ratio (Fig. 12c) from 1.4 to ∼1.7 km. Finally, we observe a strong trade-off between crustal thickness and the V_p/V_s ratio (Fig. 21c), which indicates that given a higher V_p/V_s ratio the estimated crustal thickness will be lower and vice versa.

The fact that we are unable to determine a preferred V_p/V_s ratio from our data at station R11A also holds for other stations. Figs 21(d)–(f) shows the posterior distributions of V_p/V_s ratio at stations T18A in CP, Q22A in RM and O25A in GP, respectively. Overall, we poorly constrain the V_p/V_s ratio from the data we are using. The direct effect is that when we present the 3-D model in Section 7.2, the uncertainty of crustal thickness is underestimated by up to ∼20 per cent due to the fact that the V_p/V_s ratio is set to 1.75. To improve the determination of the V_p/V_s ratio, other information such as reverberation phases arriving after 10 s in the RFs and Rayleigh
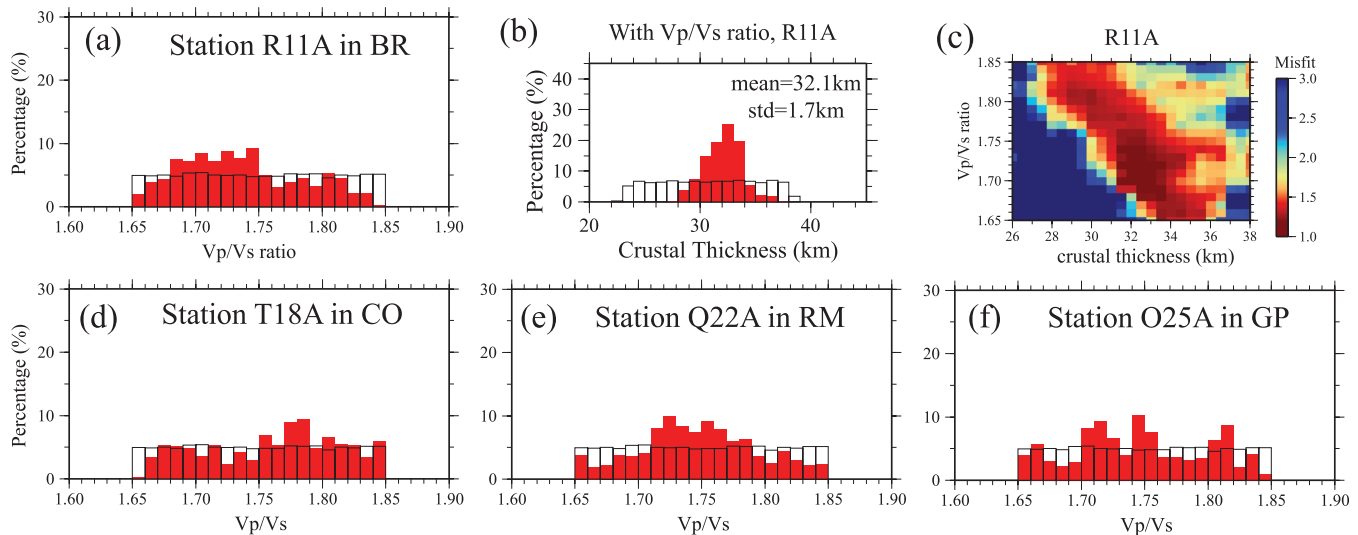
Figure 21. (a) Posterior distribution of V_p/V_s ratio when it is included as a parameter in the joint inversion. The prior distribution is shown with the white histogram outlined in black. (b) The posterior distribution of crustal thickness for station R11A from the inversion that includes V_p/V_s as a free parameter. (c) The joint misfit (χ^{joint}) is plotted as a function of crustal thickness and V_p/V_s ratio. Trade-off between crustal thickness and the V_p/V_s ratio is clear. (d)–(f) The same as (a), but for stations T18A, Q22A and O25A, respectively.

wave ellipticity and local amplification (Lin *et al.* 2012a,b) would have to be included in the Monte Carlo sampling.

8.2 Limitations of the current method and potential refinements

The procedure that we have developed is intended to provide a practical method to invert surface wave dispersion and RFs jointly over large areas. As it currently exists, the method can be applied fruitfully across large arrays that have been developed around the globe. This includes all of the USArray in the United States, as well as the Chinese Earthquake Array, the Virtual European Seismic Network, various PASSCAL experiments around the world and F-net in Japan. However, the method also serves as a framework for future enhancements and improvements. In this regard we highlight four known limitations with the method as it is currently effected that may call for modification. A fifth limitation is discussed in Section 8.1 regarding a variable V_p/V_s ratio.

First, the parametrization that we have defined is applied rigidly in the inversion. The algorithm has not been designed to sense misfit to the data and to adapt the parametrization accordingly, although other recent joint inversion algorithms include this feature (e.g. Bodin *et al.* 2011). For instance, in the inversion at station R11A (Fig. 13), a mid-crustal discontinuity was not introduced automatically to fit the negative arrival at ~1 s on the RF. An adaptive parametrization would help the algorithm fit aspects of the data that are currently being ignored, but introducing more structure would increase uncertainties and may lead to overinterpretation of the data.

Secondly, the traveltime variation of *P*-to-*S* conversions due to dipping interfaces (notably on the Moho) is not fit in our inversion and is removed in the harmonic stripping algorithm to estimate the azimuthally independent RF that we use in the joint inversion, $A_0(t)$. Not modelling the delay time variation explicitly means that the amplitude of *P*-to-*S* conversions will be underestimated if the variation is significant (i.e. ≥0.5 s). The delay time variation does appear in the $A_1(t)$ and $A_2(t)$ components of the RF that are estimated

in the harmonic stripping algorithm but which are not used in the inversion. Optimally, the algorithm would employ information that exists in these two components to correct for the underestimation of the amplitude of the phase conversions from dipping interfaces. In principle, this information as well as transverse component RF amplitudes and delay time variations could also be used to estimate the dip on the interfaces, but this information would probably have to be interpreted independently from surface wave data.

Thirdly, we do not use the RF produced from a multistation imaging technique [e.g. the Common Conversion Point (CCP) stacked RF] but rather a single-station RF which is an average of the 3-D variation near each single station. In the future, this procedure could be replaced with the RF stacked at the CCP rather than at the station. This procedure is inappropriate for the TA because the CCPs beneath nearby stations do not overlap, as Fig. 22(a) illustrates. The procedure would be appropriate for a denser array such as PASSAL or EarthScope Flexible Array experiments. Fig. 22(b) also presents a comparison between RFs computed using the TA and the CD-ROM PASSCAL experiment. The blue RFs are from three TA stations along the green transect in Fig. 22(a), and the red RFs are binned CD-ROM+TA RFs produced according to the Moho Conversion Points (MCP), where radial RFs that pierce the same bin at Moho depth are averaged laterally. The similarity between MCP RFs and the harmonic stripping $A_0(t)$ RFs demonstrate that the single station azimuthally independent RFs that we construct are consistent with the multistation RFs. A smoothed image of the multistation RFs is presented in Fig. 22(c), demonstrating the resolution that RFs from a tighter network geometry provide. Higher resolution features such as the mid-crustal signal at ~2.5 s beneath the Cheyenne Belt (CB) are not captured by the sparse TA array. However, using higher resolution RFs would necessitate accommodating the lower resolution of surface wave dispersion maps so as not to alias sharp features from the RFs into larger scale features derived in the joint inversion. It remains unclear what maximum resolution may be possible for surface waves from a tighter array spacing than the TA, for example from the Flexible Array component of USArray. It is likely, however, that surface wave resolution will always lag resolution from RFs. Although the installation of the TA has ameliorated the differential
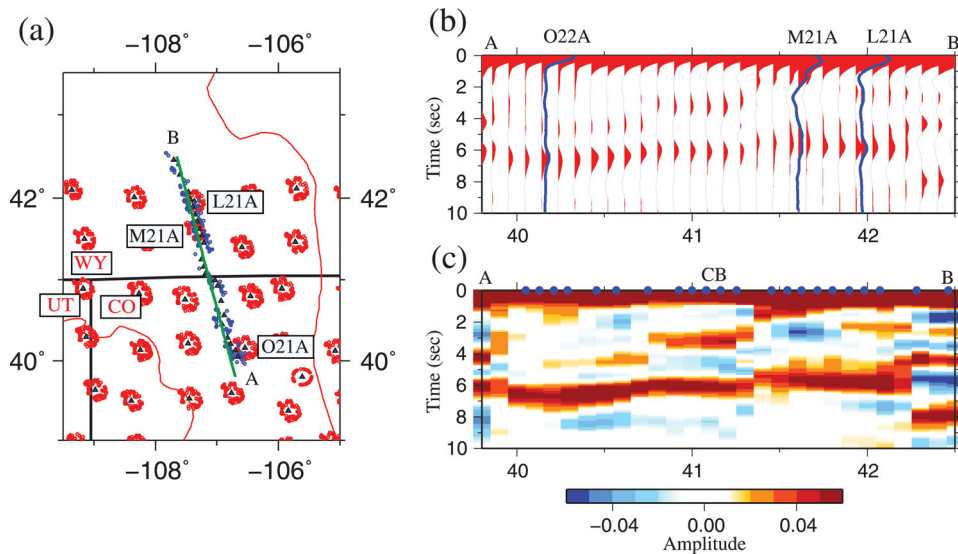
Figure 22. (a) Piercing points of the *P*-wave incident at the Moho for TA stations are shown with red dots. The piercing points for CD-ROM stations are shown with blue dots. The green line is the transect AB along the CD-ROM line from Colorado to Wyoming. Three TA stations near the transect are identified with names (L21A, M21A and O21A from north to south). State boundaries are outlined with black lines and red lines are geological provinces (Fig. 1). (b) Moho conversion point (MCP) stacked receiver functions are illustrated with red waveforms along transect AB in (a). For comparison, single-station processed receiver function s ($A_0(t)$) are shown with blue waveform for the three stations identified in (a). (c) The smoothed image of the red receiver functions in (b). Blue dots indicate the location of the CD-ROM stations. The location of the Cheyenne Belt is marked as CB.

resolution problem in the United States, the issue may ultimately need to be resolved by low-pass filtering the RFs.

Fourthly, the full error covariance matrices for surface wave dispersion data and RFs have not been utilized here. Rather, we have assumed that the matrices are diagonal (errors are independent) and have balanced the two data sets by introducing a scaling parameter (κ) that effectively normalizes the misfit found for the two data sets. Estimating the inverse covariance matrix for both data sets is not trivial, but it would improve the effectiveness of the algorithm.

9 CONCLUSIONS

We present a new method for joint inversion of surface wave dispersion data and RFs based on a Bayesian Monte Carlo scheme. When applied to RFs and surface wave data from ambient noise and earthquakes that are now emerging from extended broad-band seismic arrays, the method produces a 3-D model of the crust and uppermost mantle to a depth of about 150 km with associated uncertainties. The method is designed to be used in an automated fashion across a large number of stations and has been applied to data from 185 USArray TA stations in a geologically diverse part of the Intermountain West. The effect of the introduction of RFs to surface wave dispersion data is visualized through improvements in the posterior marginal distribution of model variables. By comparing the statistics of the posterior distributions, we find that adding RF data quantitatively improves the accuracy of estimates of Moho depth, improves the determination of the Vsv contrast across Moho and improves uppermost mantle structure. Knowledge of uppermost mantle structure is improved because the assimilation of RF data makes it possible to relax ad-hoc structural constraints that are commonly invoked in inversions based on surface wave data alone.

Although the inversion method we describe can be applied robustly across large regions, there remain aspects of the method where refinements may prove beneficial. Three are particularly noteworthy: (1) development of an adaptive parametrization, particularly in the crust where low velocity layers may exist, (2) further inves-

tigation of the estimation of the full data covariance matrix and its inverse for both RFs (covariance over time) as was done by Bodin *et al.* (2011) and surface wave dispersion (covariance over frequency), (3) extension of the RFs past 10 s to recover reverberations that may help to constrain the V_p/V_s ratio. These and other potential refinements to the method may reduce small biases that derive from current assumptions, but the current method produces results that are preferable to the use of surface wave dispersion or receiver function data alone.

REFERENCES

Abers, G.A., 1998. Array measurements of phases used in receiver-function calculations: importance of scattering, *Bull. seism. Soc. Am.,* **88,** 313–318.

Ammon, C.J., Randall, G.E. & Zandt, G., 1990. On the nonuniqueness of receiver function inversions, *J. geophys. Res.,* **95**(B10), 15 303–15 318, doi:10.1029/JB095iB10p15303.

Ammon, C.J. & Zandt, G., 1993. Receiver structure beneath the southern mojave block, California, *Bull. seism. Soc. Am.,* **83,** 737–755.

An, M. & Assumpção, M.S., 2004. Multi-objective inversion of surface waves and receiver functions by competent genetic algorithm applied to the crustal structure of the Paraná Basin, SE Brazil, *Geophys. Res. Lett.,* **31,** L05 615, doi:10.1029/2003GL019179.

Bailey, I.W., Miller, M.S., Liu, K. & Levander, A., 2012. V_s and density structure beneath the Colorado Plateau constrained by gravity anomalies and joint inversions of receiver function and phase velocity data, *J. geophys. Res.,* **117,** B02 313, doi:10.1029/2011JB008522.

Bannister, S., Yu, J., Leitner, B. & Kennett, B.L.N., 2003. Variations in crustal structure across the transition from West to East Antarctica, Southern Victoria Land, *Geophys. J. Int.,* **155,** 870–884.

Bassin, C., Laske, G. & Masters, G., 2000. The current limits of resolution for surface wave tomography in North America, *EOS Trans AGU,* **81,** F897.

Basuyau, C. & Tiberi, C., 2011. Imaging lithospheric interfaces and 3D structures using receiver functions, gravity, and tomography in a common inversion scheme, *Comput. Geosci.,* **37,** 1381–1390.

Bensen, G.D., Ritzwoller, M.H., Barmin, M.P., Levshin, A.L., Lin, F., Moschetti, M.P., Shapiro, N.M. & Yang, Y., 2007. Processing seismic ambient noise data to obtain reliable broad-band surface wave dispersion measurements, *Geophys. J. Int.,* **169,** 1239–1260.

Bensen, G.D., Ritzwoller, M.H. & Yang, Y., 2009. A 3D shear velocity model of the crust and uppermost mantle beneath the United States from ambient seismic noise, *Geophys. J. Int.,* **177**(3), 1177–1196.

Bianchi, I., Park, J., Piana Agostinetti, N. & Levin, V., 2010. Mapping seismic anisotropy using harmonic decomposition of receiver functions: an application to Northern Apennines, Italy, *J. geophys. Res.,* **115,** B12 317, doi:10.1029/2009JB007061.

Bodin, T., Sambridge, M., Tkalčić, H., Arroucau, P., Gallagher, K. & Rawlinson, N., 2012. Transdimensional inversion of receiver functions and surface wave dispersion, *J. geophys. Res.,* **117,** B02 301, doi:10.1029/2011JB008560.

Bostock, M.G., 1998. Mantle stratigraphy and evolution of the Slave province, *J. geophys. Res.,* **103**(B9), 21 183–21 200, doi:10.1029/98JB01069.

Cassidy, J.F., 1992. Numerical experiments in broad-band receiver function-analysis, *Bull. seism. Soc. Am.,* **82**(3), 1453–1474.

Chang, S.J., Baag, C.E. & Langston, C.A., 2004. Joint analysis of teleseismic receiver functions and surface wave dispersion using the genetic algorithm, *Bull. seism. Soc. Am.,* **94,** 691–704.

Christensen, N.I. & Mooney, W.D., 1995. Seismic velocity structure and composition of the continental crust: a global view, *J. geophys. Res.,* **100**(B6), 9761–9788.

Clitheroe, G., Gudmundsson, O. & Kennett, B.L.N., 2000. The crustal thickness of Australia, *J. geophys. Res.,* **105**(B6), 13 697–13 713, doi:10.1029/1999JB900317.

Crotwell, H.P. & Owens, T.J., 2005. Automated receiver function processing, *Seismol. Res. Lett.,* **76**(6), 702–709.

Du, Z.J. & Foulger, G.R., 1999. The crustal structure beneath the northwest fjords, Iceland, from receiver functions and surface waves, *Geophys. J. Int.,* **139,** 419–432.

Dziewonski, A. & Anderson, D., 1981. Preliminary reference Earth model, *Phys. Earth planet. Inter.,* **25**(4), 297–356.

Endrun, B., Meier, T., Bischoff, M. & Harjes, H.P., 2004. Lithospheric structure in the area of Crete constrained by receiver functions and dispersion analysis of Rayleigh phase velocities, *Geophys. J. Int.,* **158,** 592–608.

Frederiksen, A.W. & Bostock, M.G., 2000. Modelling teleseismic waves in dipping anisotropic structures, *Geophys. J. Int.,* **141,** 401–412.

Frederiksen, A.W., Folsom, H. & Zandt, G., 2003. Neighbourhood inversion of teleseismic P_s conversions for anisotropy and layer dip, *Geophys. J. Int.,* **155,** 200–212.

Gilbert, H.J. & Sheehan, A.F., 2004. Images of crustal variations in the intermountain west, *J. geophys. Res.,* **109,** B03 306, doi:10.1029/2003JB002730.

Girardin, N. & Farra, V., 1998. Azimuthal anisotropy in the upper mantle from observations of P-to-S converted phases: application to southeast Australia, *Geophys. J. Int.,* **133,** 615–629.

Gok, R., Pasyanos, M.E. & Zor, E., 2007. Lithospheric structure of the continent-continent collision zone: eastern Turkey, *Geophys. J. Int.,* **169,** 1079–1088.

Gorman, A.R. *et al.*, 2002. Deep Probe: Imaging the roots of western North America, *Can. J. Earth Sci.,* **39**(3), 375–398.

Hetenyi, G. & Bus, Z., 2007. Shear wave velocity and crustal thickness in the Pannonian Basin from receiver function inversions at four permanent stations in Hungary, *J. Seismol.,* **11,** 405–414.

Horspool, N.A., Savage, M.K. & Bannister, S., 2006. Implications for intraplate volcanism and back-arc deformation in northwestern New Zealand, from joint inversion of receiver functions and surface waves, *Geophys. J. Int.,* **166,** 1466–1483.

Jones, C.H. & Phinney, R.A., 1998. Seismic structure of the lithosphere from teleseismic converted arrivals observed at small arrays in the southern Sierra Nevada and vicinity, California, *J. geophys. Res.,* **103**(B5), 10 065–10 090, doi:10.1029/97JB03540.

Julia, J., Ammon, C.J. & Herrmann, R.B., 2003. Lithospheric structure of the Arabian Shield from the joint inversion of receiver functions and surface-wave group velocities, *Tectonophysics,* **371,** 1–21.

Julia, J., Ammon, C.J., Herrmann, R.B. & Correig, A.M., 2000. Joint inversion of receiver function and surface wave dispersion observations, *Geophys. J. Int.,* **143,** 99–112.

Kanamori, H. & Anderson, D., 1977. Importance of physical dispersion in surface wave and free oscillation problems: review, *Revs. Geophys. Space Phys.,* **15**(1), 105–112.

Karato, S., 1993. Importance of anelasticity in the interpretation of seismic tomography, *Geophys. Res. Lett.,* **20**(15), 1623–1626, doi:10.1029/93GL01767.

Khan, A., Zunino, A. & Deschamps, F., 2011. The thermo-chemical and physical structure beneath the North American continent from Bayesian inversion of surface-wave phase velocities, *J. geophys. Res.,* **116,** B09 304, doi:10.1029/2011JB008380.

Langston, C.A., 1979. Structure under Mount Rainier, Washington, inferred from teleseismic body waves, *J. geophys. Res.,* **84**(B9), 4749–4762, doi:10.1029/JB084iB09p04749.

Last, R.J., Nyblade, A.A., Langston, C.A. & Owens, T.J., 1997. Crustal structure of the East African Plateau from receiver functions and Rayleigh wave phase velocities, *J. geophys. Res.,* **102**(B11), 24 469–24 483, doi:10.1029/97JB02156.

Lawrence, J.F. & Wiens, D.A., 2004. Combined receiver-function and surface wave phase-velocity inversion using a niching genetic algorithm: application to Patagonia, *Bull. seism. Soc. Am.,* **94,** 977–987.

Levander, A., Schmandt, B., Miller, M.S., Liu, K., Karlstrom, K.E., Crow, R.S., Lee, C.T.A. & Humphreys, E.D., 2011. Continuing Colorado plateau uplift by delamination-style convective lithospheric downwelling, *Nature,* **472**(7344), 461–465.

Levin, V. & Park, J., 1997. P-SH conversions in a flat-layered medium with anisotropy of arbitrary orientation, *Geophys. J. Int.,* **131,** 253–266.

Levshin, A.L. & Ritzwoller, M.H., 1995. Characteristics of surface waves generated by events on and near the Chinese nuclear test site, *Geophys. J. Int.,* **123,** 131–149.

Levin, V., Shapiro, N.M., Park, J. & Ritzwoller, M.H., 2002. Seismic evidence for catastrophic slab loss beneath Kamchatka, *Nature,* **418,** 763–767.

Levshin, A.L., Ritzwoller, M.H. & Shapiro, N.M., 2005. The use of crustal higher modes to constrain crustal structure across Central Asia, *Geophys. J. Int.,* **160,** 961–972.

Ligorria, J.P. & Ammon, C.J., 1999. Iterative deconvolution and receiver-function estimation, *Bull. seism. Soc. Am.,* **89**(5), 1395–1400.

Lin, F.C., Moschetti, M.P. & Ritzwoller, M.H., 2008. Surface wave tomography of the western United States from ambient seismic noise: Rayleigh and Love wave phase velocity maps, *Geophys. J. Int.,* **173,** 281–298.

Lin, F.C. & Ritzwoller, M.H., 2011. Helmholtz surface wave tomography for isotropic and azimuthally anisotropic structure, *Geophys. J. Int.,* **186,** 1104–1120.

Lin, F.C., Ritzwoller, M.H., Yang, Y., Moschetti, M.P. & Fouch, M.J., 2011. Complex and variable crustal and uppermost mantle seismic anisotropy in the western United States, *Nat. Geosci.,* **4**(1), 55–61.

Lin, F.C., Ritzwoller, M.H. & Snieder, R., 2009. Eikonal tomography: surface wave tomography by phase front tracking across a regional broadband seismic array, *Geophys. J. Int.,* **177,** 1091–1110.

Lin, F.C., Tsai, V. & Ritzwoller, M.H., 2012a. The local amplification of surface waves: a new observable to constrain elastic velocities, density, and anelastic attenuation, *J. geophys. Res.,* **117**(B06302), doi:10.1029/2012JB009208.

Lin, F.C., Schmandt, B. & Tsai, V.C., 2012b. Joint inversion of Rayleigh wave phase velocity and ellipticity using USArray: constraining velocity and density structure in the upper crust, *Geophys. Res. Lett.,* **39**(L12303), doi:10.1029/2012GL052196.

Liu, Q.Y., Li, Y., Chen, J.H., van der Hilst, R.D., Guo, B.A., Wang, J., Qi, S.H. & Li, S.C., 2010. Joint inversion of receiver function and ambient noise based on Bayesian theory, *Chin. J. Geophys.-Chin. Ed.,* **53,** 2603–2612.

Lowry, A.R. & Perez-Gussinye, M., 2011. The role of crustal quartz in controlling Cordilleran deformation, *Nature,* **471,** 353–357.

Lucente, F.P., Piana Agostinetti, N., Moro, M., Selvaggi, G. & Di Bona, M., 2005. Possible fault plane in a seismic gap area of the southern Apennines (Italy) revealed by receiver function analysis, *J. geophys. Res.,* **110,** B04 307, doi:10.1029/2004JB003187.

Maraschini, M. & Foti, S., 2010. A Monte Carlo multimodal inversion of surface waves, *Geophys. J. Int.,* **182,** 1557–1566.

Megnin, C. & Romanowicz, B., 2000. The three-dimensional shear velocity structure of the mantle from the inversion of body, surface and higher-mode waveforms, *Geophys. J. Int.,* **143**(3), 709–728.

Molnar, S., Dosso, S.E. & Cassidy, J.F., 2010. Bayesian inversion of microtremor array dispersion data in southwestern British Columbia, *Geophys. J. Int.,* **183,** 923–940.

Mooney, W.D. & Kaban, M.K., 2010. The North American upper mantle: density, composition, and evolution, *J. geophys. Res.,* **115,** B12 424, doi:10.1029/2010JB000866.

Moorkamp, M., Jones, A.G. & Fishwick, S., 2010. Joint inversion of receiver functions, surface wave dispersion, and magnetotelluric data, *J. geophys. Res.,* **115,** B04 318, doi:10.1029/2009JB006369.

Moschetti, M.P., Ritzwoller, M.H. & Lin, F.C., 2010. Seismic evidence for widespread crustal deformation caused by extension in the western USA, *Nature,* **464**(7290), 885–889.

Moschetti, M.P., Ritzwoller, M.H. & Shapiro, N.M., 2007. Surface wave tomography of the western United States from ambient seismic noise: Rayleigh wave group velocity maps, *Geochem. Geophys. Geosyst.,* **8**(Q08010), doi:10.1029/2007GC001655.

Moschetti, M.P., Ritzwoller, M.H., Lin, F.C. & Yang, Y., 2010a. Crustal shear wave velocity structure of the western United States inferred from ambient seismic noise and earthquake data, *J. geophys. Res.-Solid Earth,* **115**(B10306), doi:10.1029/2010JB007448.

Moschetti, M.P., Ritzwoller, M.H., Lin, F.C. & Yang, Y., 2010b. Crustal shear velocity structure of the western US inferred from amient noise and earthquake data, *J. geophys. Res.,* **115,** B10 306, doi:10.1029/2010JB007448.

Mosegaard, K. & Tarantola, A., 1995. Monte Carlo sampling of solutions to inverse problems, *J. geophys. Res.,* **100**(B7), 12 431–12 447, doi:10.1029/94JB03097.

Mosegaard, K. & Sambridge, M., 2002. Monte Carlo analysis of inverse problems, *Inverse Probl.,* **18,** 29–54.

Nicholson, T., Bostock, M. & Cassidy, J.F., 2005. New constraints on subduction zone structure in northern Cascadia, *Geophys. J. Int.,* **161,** 849–859.

Ozalaybey, S., Savage, M.K., Sheehan, A.F., Louie, J.N. & Brune, J.N., 1997. Shear-wave velocity structure in the northern Basin and Range province from the combined analysis of receiver functions and surface waves, *Bull. seism. Soc. Am.,* **87,** 183–199.

Pasyanos, M.E., Tkalcic, H., Gok, R., Al-Enezi, A. & Rodgers, A.J., 2007. Seismic structure of Kuwait, *Geophys. J. Int.,* **170,** 299–312.

Piana Agostinetti, N., Lucente, F.P., Selvaggi, G. & Di Bona, M., 2002. Crustal structure and Moho geometry beneath the Northern Apennines (Italy), *Geophys. Res. Lett.,* **29**(20), 1999, doi:10.1029/2002GL015109.

Piana Agostinetti, N. & Chiarabba, C., 2008. Seismic structure beneath Mt Vesuvius from receiver function analysis and local earthquakes tomography: evidences for location and geometry of the magma chamber, *Geophys. J. Int.,* **175,** 1298–1308.

Piana Agostinetti, N. & Malinverno, A., 2010. Receiver function inversion by trans-dimensional Monte Carlo sampling, *Geophys. J. Int.,* **181,** 858–872.

Pollitz, F.F., 2008. Observations and interpretation of fundamental mode Rayleigh wavefields recorded by the Transportable Array (USArray), *Geophys. J. Int.,* **173,** 189–204.

Pollitz, F.F. & Snoke, J.A., 2010. Rayleigh-wave phase-velocity maps and three dimensional shear velocity structure of the western US from local non-plane surface wave tomography, *Geophys. J. Int.,* **180,** 1153–1169.

Ritzwoller, M.H. & Levshin, A.L., 1998. Eurasian surface wave tomography: group velocities, *J. geophys. Res.,* **103,** 4839–4878.

Ritzwoller, M.H., Levshin, A.L., Ratnikova, L.I. & Egorkin, A.A., 1998. Intermediate period group velocity maps across Central Asia, Western China, and parts of the Middle East, *Geophys. J. Int.,* **134,** 315–328.

Ritzwoller, M.H., Shapiro, N.M., Levshin, A.L. & Leahy, G.M., 2001. Crustal and upper mantle structure beneath Antarctica and surrounding oceans, *J. geophys. Res.,* **106**(B12), 30 645–30 670, doi:10.1029/2001JB000179.

Ritzwoller, M.H., Shapiro, N.M. & Leahy, G.M., 2003. A resolved mantle anomaly as the cause of the Australian-Antarctic Discordance, *J. geophys. Res.,* **108**(B12), 2559, doi:10.1029/2003JB002522.

Ritzwoller, M.H., Shapiro, N.M. & Zhong, S., 2004. Cooling history of the Pacific lithosphere, *Earth planet. Sci. Lett.,* **226,** 69–84.

Ritzwoller, M.H., Lin, F.C. & Shen, W., 2011. Ambient noise tomography with a large seismic array, *Compte Rendus Geosci.,* 13, doi:10.1016/j.crte.2011.03.007.

Roy, M., Jordan, T.H. & Pederson, J., 2009. Colorado Plateau magmatism and uplift by warming of heterogeneous lithosphere, *Nature,* **459,** 978–982.

Salah, M.K., Chang, S.J. & Fonseca, J., 2011. Crustal structure beneath the Lower Tagus Valley, southwestern Iberia using joint analysis of teleseismic receiver functions and surface-wave dispersion, *Geophys. J. Int.,* **184,** 919–933.

Sambridge, M., 1999a. Geophysical inversion with a neighbourhood algorithm—I. Searching a parameter space, *Geophys. J. Int.,* **138,** 479–494.

Sambridge, M., 1999b. Geophysical inversion with a neighbourhood algorithm—II. Appraising the ensemble, *Geophys. J. Int.,* **138,** 727–746.

Sambridge, M., 2001. Finding acceptable models in nonlinear inverse problems using a neighbourhood algorithm, *Inverse Probl.,* **17,** 387–403.

Sambridge, M. & Mosegaard, K., 2002. Monte Carlo methods in geophysical inverse problems, *Rev. Geophys.,* **40,** 1–29.

Savage, M.K., 1998. Lower crustal anisotropy or dipping boundaries? Effects on receiver functions and a case study in New Zealand, *J. geophys. Res.,* **103,** 15 069–15 087.

Schultz, C.A., Myers, S.C., Hipp, J. & Young, C.J., 1999. Nonstationary Bayesian kriging: a predictive technique to generate spatial corrections for seismic detection, location and identification, *Phys. Earth planet. Inter.,* **113,** 321–338.

Shapiro, N.M., Campillo, M., Stehly, L. & Ritzwoller, M.H., 2005. High-resolution surface-wave tomography from ambient seismic noise, *Science,* **307,** 1615–1618.

Shapiro, N.M. & Ritzwoller, M.H., 2002. Monte-Carlo inversion for a global shear-velocity model of the crust and upper mantle, *Geophys. J. Int.,* **151,** 88–105.

Shapiro, N.M., Ritzwoller, M.H. & Engdahl, E.R., 2008. Structural context of the great Sumatra-Andaman Islands earthquake, *Geophys. Res. Lett.,* **35,** L05 301, doi:10.1029/2008GL033381.

Sheehan, A.F., Jones, C.H., Savage, M.K., Ozalaybey, S. & Schneider, J.M., 1997. Contrasting lithospheric structure between the Colorado Plateau and Great Basin: initial results from Colorado Plateau—Great

Basin PASSCAL Experiment, *Geophys. Res. Lett.,* **24**(21), 2609–2612, doi:10.1029/97GL02782.

Shibutani, T., Sambridge, M. & Kennett, B., 1996. Genetic algorithm inversion for receiver functions with application to crust and uppermost mantle structure beneath eastern Australia, *Geophys. Res. Lett.,* **23**(14), 1829–1832, doi:10.1029/96GL01671.

Socco, L.V. & Boiero, D., 2008. Improved Monte Carlo inversion of surface wave data, *Geophys. Prospect.,* **56,** 357–371.

Tarantola, A. & Valette, B., 1982. Generalized nonlinear inverse problems solved using the least squares criterion, *Rev. Geophys.,* **20**(2), 219–232, doi:10.1029/RG020i002p00219.

Tkalčić, H., Pasyanos, M.E., Rodgers, A.J., Gök, R., Walter, W.R. & Al-Amri, A., 2006. A multistep approach for joint modeling of surface wave dispersion and teleseismic receiver functions: implications for lithospheric structure of the Arabian Peninsula, *J. geophys. Res.,* **111,** B11 311, doi:10.1029/2005JB004130.

Tokam, A.P.K., Tabod, C.T., Nyblade, A.A., Julia, J., Wiens, D.A. & Pasyanos, M.E., 2010. Structure of the crust beneath Cameroon, West Africa, from the joint inversion of Rayleigh wave group velocities and receiver functions, *Geophys. J. Int.,* **183,** 1061–1076.

Villasenor, A., Ritzwoller, M.H., Levshin, A.L., Barmin, M.P., Engdahl, E.R., Spakman, W. & Trampert, J., 2001. Shear velocity structure of Central Eurasia from inversion of surface wave velocities, *Phys. Earth planet. Inter.,* **123**(2–4), 169–184.

Vinnik, L.P., 1977. Detection of waves converted from P to SV in the mantle, *Phys. Earth planet. Inter.,* **15,** 39–45.

Vinnik, L.P., Aleshin, I.M., Kaban, M.K., Kiselev, S.G., Kosarev, G.L., Oreshin, S.I. & Reigber, C., 2006. Crust and mantle of the Tien Shan from data of the receiver function tomography, *Izvestiya-Phys. Solid Earth,* **42,** 639–651.

Vinnik, L.P., Reigber, C., Aleshin, I.M., Kosarev, G.L., Kaban, M.K., Oreshin, S.I. & Roecker, S.W., 2004. Receiver function tomography of the central Tien Shan, *Earth planet. Sci. Lett.,* **225,** 131–146.

Wilson, C.K., Jones, C.H. & Gilbert, H.J., 2003. Single-chamber silicic magma system inferred from shear wave discontinuities of the crust and uppermost mantle, Coso geothermal area, California, *J. geophys. Res.,* **108**(B5), doi:10.1029/2002JB001798.

Yang, Y. & Forsyth, D., 2006. Regional tomographic inversion of the amplitude and phase of Rayleigh waves with 2-D sensitivity kernels, *Geophys. J. Int.,* **166,** 1148–1160.

Yang, Y.J., Ritzwoller, M.H., Levshin, A.L. & Shapiro, N.M., 2007. Ambient noise Rayleigh wave tomography across Europe, *Geophys. J. Int.,* **168,** 259–274.

Yang, Y. & Ritzwoller, M.H., 2008. Teleseismic surface wave tomography in the western U.S. using the Transportable Array component of USArray, *Geophys. Res. Lett.,* **35,** L04 308, doi:10.1029/2007GL032278.

Yang, Y., Li, A. & Ritzwoller, M.H., 2008a. Crustal and uppermost mantle structure in southern Africa revealed from ambient noise and teleseismic tomography, *Geophys. J. Int.,* doi:10.1111/j.1365-246X.2008.03779.x.

Yang, Y., Ritzwoller, M.H., Lin, F.-C., Moschetti, M.P. & Shapiro, N.M., 2008b. Structure of the crust and uppermost mantle beneath the western United States revealed by ambient noise and earthquake tomography, *J. geophys. Res.,* **113,** B12 310, doi:10.1029/2008JB005833.

Yang, Y., Ritzwoller, M.H. & Jones, C.H., 2011. Crustal structure determined from ambient noise tomography near the magmatic centers of the Coso region, southeastern California, *Geochem. Geophys. Geosyst.,* **12,** Q02 009, doi:10.1029/2010GC003362.

Yang, Y., Ritzwoller, M.H., Zheng, Y., Shen, W., Levshin, A.L. & Xie, Z., 2012. A synoptic view of the distribution and connectivity of the mid-crustal low velocity zone beneath Tibet, *J. geophys. Res.,* **117,** B04 303, doi:10.1029/2011JB008810.

Yao, H.J., van der Hilst, R.D. & de Hoop, M.V., 2006. Surface-wave array tomography in SE Tibet from ambient seismic noise and two-station analysis—I. Phase velocity maps, *Geophys. J. Int.,* **166,** 732–744.

Yoo, H.J., Herrmann, R.B., Cho, K.H. & Lee, K., 2007. Imaging the three-dimensional crust of the Korean Peninsula by joint inversion of surface-wave dispersion and teleseismic receiver functions, *Bull. seism. Soc. Am.,* **97,** 1002–1011.

Yoshizawa, K. & Kennett, B.L.N., 2002. Non-linear waveform inversion for surface waves with a neighbourhood algorithm—application to multimode dispersion measurements, *Geophys. Int.,* **149,** 118–133.

Zhao, L.S., Sen, M.K., Stoffa, P. & Frohlich, C., 1996. Application of very fast simulated annealing to the determination of the crustal structure beneath Tibet, *Geophys. J. Int.,* **125,** 355–370.

Zheng, X.F., Yao, Z.X., Liang, J.H. & Zheng, J., 2010. The role played and opportunities provided by IGP DMC of China National Seismic Network in Wenchuan earthquake disaster relief and researches, *Bull. seism. Soc. Am.,* **100**(5B), 2866–2872.

Zheng, Y., Shen, W., Zhou, L., Yang, Y., Xie, Z. & Ritzwoller, M.H., 2011. Crust and uppermost mantle beneath the North China Craton, northeastern China, and the Sea of Japan from ambient noise tomography, *J. geophys. Res.,* **116,** B12 312, doi:10.1029/2011JB008637.

Zhou, L., Xie, J., Shen, W., Zheng, Y., Yang, Y., Shi, H. & Ritzwoller, M.H., 2012. The structure of the crust and uppermost mantle beneath South China from ambient noise and earthquake tomography, *Geophys. J. Int.,* **159,** 1565–1583.

Zhu, L. & Kanamori, H., 2000. Moho depth variation in southern California from teleseismic receiver functions, *J. geophys. Res.,* **105**(B2), 2969–2980, doi:10.1029/1999JB900322.

APPENDIX: CONSTRUCTING AZIMUTHALLY INDEPENDENT RECEIVER FUNCTIONS BY 'HARMONIC STRIPPING'

A1 Receiver function data collection

We apply the time-domain iterative deconvolution method (Ligorria & Ammon 1999) to a time window between 20 s before and 30 s after the predicted *P*-wave arrival to calculate radial component receiver functions and filtered to produce a pulse width of approximately 1 s. *P*-waves at different distances have different incidence angles that affect both the timing and the amplitude of the *P*-to-*S* converted phase (Levin & Park 1997; Bostock 1998; Jones & Phinney 1998). We make corrections to the receiver functions in both time and amplitude by normalizing to a reference slowness of 0.06 deg s^{-1}. The correction is based on a two-layer model with a crustal layer ($V_s = 3.7$ km s^{-1}) of 40 km thickness and a half-space mantle layer ($V_s = 4.3$ km s^{-1}). Because this correction is designed to normalize the *P*-to-*S* conversion at the Moho discontinuity and reverberated phases have a different time and amplitude dependence on incidence angle, we discard the portion of the receiver function beyond 10 s after the direct *P*-signal. Any shallow sedimentary multiples that are present in the receiver functions are still retained in this time-series, but they are stacked down because of their different moveout behaviour. After application of this correction, remaining variations in receiver functions over azimuth are mainly due to systematic effects such as dipping interfaces or anisotropy beneath the receiver, structural heterogeneity, scattering (Abers 1998) and random noise in the seismograms. An example of quality controlled receiver functions observed at station R11A in the Basin and Range region is shown in Fig. A1(a), where the receiver functions are arrayed according to event backazimuth.

A2 Harmonic stripping

Harmonic analysis of receiver functions is designed to analyse the azimuthal dependence of receiver function arrivals such that azimuthally smooth structural affects are detected and removed, notably potential dipping interfaces (e.g. Savage 1998; Bianchi *et al.*
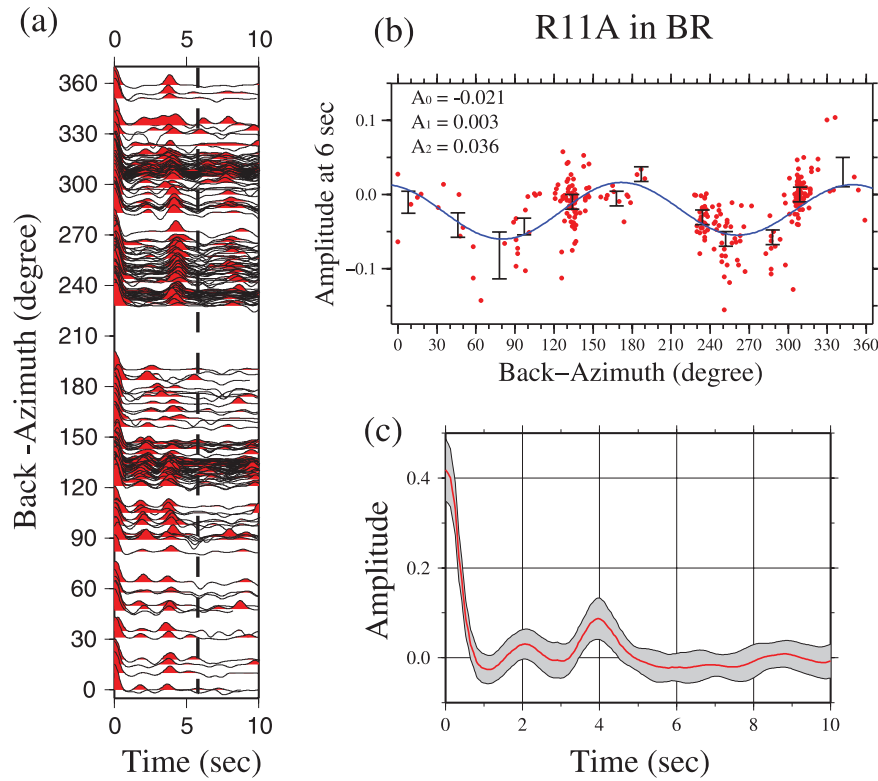
Figure A1. (a) Raw receiver function (RF) waveforms for station R11A in the Basin and Range are plotted as a function of backazimuth, where 6 s time is identified with the dashed line. (b) Red dots are RF amplitude measured at 6 s time with azimuthally binned amplitudes plotted with black error-bars. The harmonic fitting result is shown with the blue curve and the amplitudes of the estimated coefficients A_0, A_1 and A_2 (eq. (A1)) are shown. (c) The azimuthally independent $A_0(t)$ component of the RF that results from harmonic stripping is plotted (red curve) with the uncertainty range (grey corridor), which is the rms of the residual remaining after the harmonic fitting (eq. (A2)).

2010) and azimuthal anisotropy (e.g. Girardin & Farra 1998). This is possible because both dipping interfaces and anisotropy generate sinusoidal variations as a function of backazimuth with different azimuthal periodicity (Jones & Phinney 1998). Decomposition into azimuthal components isolates contributions from horizontal symmetry axis anisotropy (two amplitude peaks and troughs over the complete backazimuthal range) and a much stronger plunging symmetry axis anisotropy signal or dipping isotropic interfaces (one peak and trough over backazimuth). The azimuthally independent component of the resulting harmonic function represents an isotropic, horizontally layered average of structure that is relatively unbiased by uneven and incomplete backazimuthal sampling, and is useful for joint inversion with surface waves:

$$H(\theta, t) = A_0(t) + A_1(t) \sin[\theta + \theta_1(t)]$$
$$+ A_2(t) \sin[2\theta + \theta_2(t)], \qquad (A1)$$

where the A_i ($i = 0, 1, 2$) are amplitudes of the three harmonic components, and the θ_i are initial phases for the azimuthally dependent components. An example of the amplitude versus backazimuth for the receiver functions observed at TA station R11A at 6 s is shown in Fig. A1(b).

Under realistic circumstances where dipping interfaces and anisotropy beneath the receiver frequently exist, A_1 and A_2 will not be zero whereas A_0 will be the azimuthally independent receiver function (Fig. A1c). Here, $A_0(t)$ is treated as the receiver function that is sensitive to the average horizontally layered isotropic structure beneath the receiver and is, therefore, comparable to surface wave dispersion data. We refer to the method by which the azimuthally independent receiver function, $A_0(t)$, is estimated by

fitting and removing the harmonic function $H(\theta, t)$ from the raw receiver functions as 'harmonic stripping'.

To estimate the uncertainty $s(t)$ in $A_0(t)$ we use the RMS difference over azimuth between the observed receiver functions and the harmonic function defined by eq. (A1),

$$s(t) = \left\{ N^{-1} \sum_{i=1}^{N} [R_i(\theta_i, t) - H(\theta_i, t)]^2 \right\}^{1/2}. \qquad (A2)$$

Here, $R_i(\theta_i, t)$ represents an observed quality-controlled (see below) receiver function at discrete azimuth θ_i for event i and N is the number of such receiver functions. This residual is a measure of the difference between the red dots and the fit line in Fig. A1(b), averaged over azimuth. Fig. 4(c) shows the difference between the observed receiver functions and the harmonic function for station R11A. The uncertainty estimated in this way is presented in Fig. A1(c) as a one standard deviation corridor about $A_0(t)$. Examples of receiver functions and uncertainties are presented for other stations in Fig. 5.

The RMS of the residuals over time for the receiver functions in Fig. A1(c) is ∼0.035, which is about twice the estimated noise in receiver functions (∼ 0.015) found by Bodin *et al.* (2012), and is also about twice the RMS of the misfit between the observed receiver function and the receiver function from the best fitting model. We believe, therefore, that this definition of the uncertainty in receiver functions overestimates the uncertainty of $A_0(t)$ that is produced from harmonic stripping. To compensate for this overestimation of the uncertainties, we make two corrections. First, we reduce uncertainties in the azimuthally independent receiver function between 3 and 8 s by a factor of two to emphasize the fit to the *P*-to-*S*
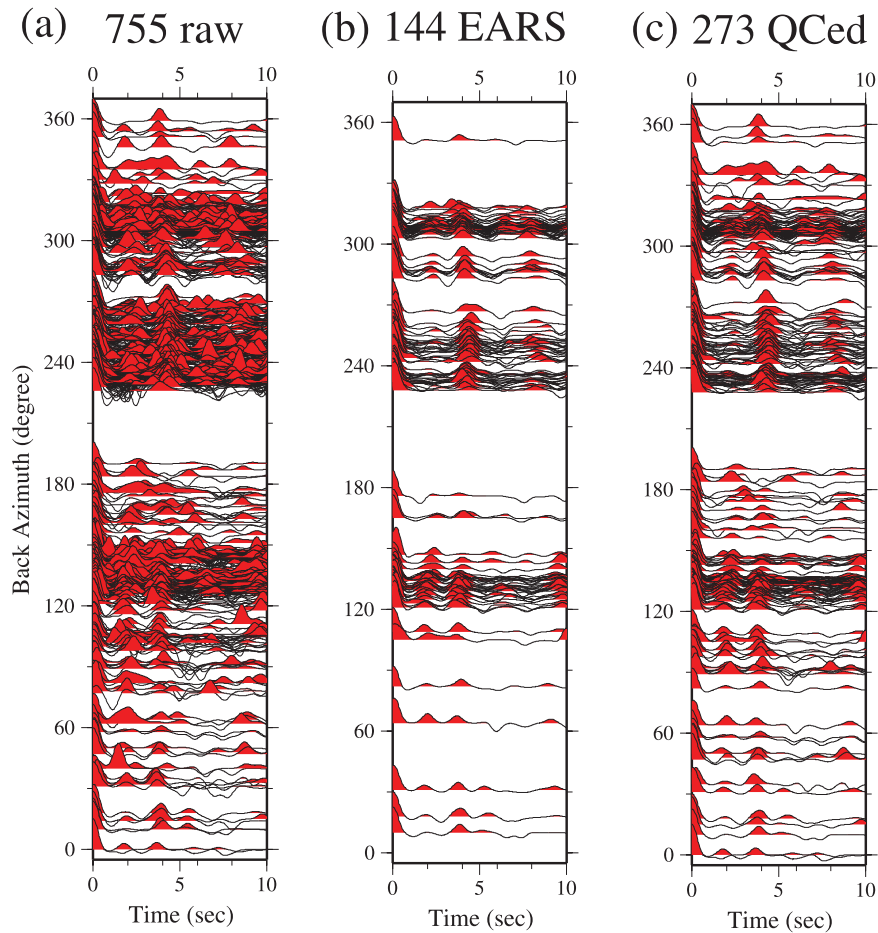
Figure A2. (a) The 755 raw receiver functions (RFs) are plotted along backazimuth for TA station R11A. (b) The same as (a), but for the 144 RFs in (a) that have been quality controlled by EARS. (c) The 273 quality controlled RFs including the 144 RFs from EARS and an additional 129 RFs from (a) that are consistent with them.

converted signal in the receiver functions. Subsequent plots of receiver function uncertainties possess this reduction (Figs 5, 13 and 16). Secondly, we introduce a factor (κ) in the Monte Carlo inversion that acts to normalize the misfit to the surface wave and receiver function data as seen in eq. (5). The determination of the appropriate value for κ is discussed in Section 6.1.

A3 Quality control (QC)

The observed azimuthally dependent receiver functions, $R_i(\theta_i, t)$, that go into the harmonic stripping procedure must first be quality controlled. We build on the quality control applied to the Earthscope Automated Receiver Study (EARS) database and seek only receiver functions that are consistent with the automatically QC'ed receiver functions from EARS used in their stacking procedure that are available through IRIS (Crotwell & Owens 2005). The EARS data selection criterion is quite conservative (variance reduction in the iterative deconvolution of at least 80 per cent) so that significant azimuthal gaps are left in the EARS receiver function station sets (e.g. Fig. A2b). We seek to expand the receiver function database relative to the EARS database, but retain the quality of the constitutive receiver functions in the EARS database. To control the quality of the raw receiver functions (e.g. Fig. A2a for station R11A) we, first, perform harmonic stripping using the EARS data alone and get a preliminary estimate of the harmonic function $\hat{H}(\theta,t)$. Then we

consider each of the raw receiver functions in the database, filtered identically with those in the EARS database (the time windows used in the deconvolution differ somewhat between the EARS and our database, but this has little effect on the resulting receiver functions). Those that are similar to the preliminary estimate $\hat{H}(\theta,t)$ from EARS are retained, whereas those that are dissimilar are rejected. There are numerous ways to define similarity that would yield similar results. We define the difference functional between each raw receiver function at azimuth θ_i and the preliminary estimate of the harmonic fit from EARS as follows:

$$D(\theta_i) = \left\{ M^{-1} \sum_{j=1}^{M} \left[R_i(\theta_i, t_j) - \hat{H}(\theta_i, t_j) \right]^2 \right\}^{1/2}, \qquad \text{(A3)}$$

where M is the number of discrete time points in the receiver functions. We find that if we retain receiver functions where $D(\theta_i) < 0.05$, then we retain many more receiver functions than in the EARS database but at the same time do not greatly increase the noise level of the database. Fig. A2(c) presents the results of this QC procedure for TA station R11A. The resulting database has been expanded by about a factor of two relative to EARS, but most of the noisy raw receiver functions have been discarded. We refer to this as the QC'ed receiver function database and it is used to estimate the final harmonic fit and azimuthally independent receiver function $A_0(t)$ with associated uncertainties $s(t)$.

Table A1. Horizontally layered isotropic model M_0.

Layer	Vsv (m s^{-1})	V_p (m s^{-1})	Density (kg m^{-3})	Thickness (km)
1	3500	6125	2746	45
2	4300	7525	3350	$\sim$

A4 Synthetic test of harmonic stripping

The goal of harmonic stripping is to remove the azimuthal periodicity of receiver function waveforms due to dipping interfaces, azimuthal anisotropy, or other structures beneath the receiver. Synthetic tests are presented here to illuminate the capabilities of harmonic stripping to remove structural effects and recover the azimuthally independent receiver function for a horizontally layered, isotropic effective medium.

First, we test the affects of structures that produce azimuthally smooth signals in the receiver functions; namely (1) a dipping Moho interface and (2) crustal azimuthal anisotropy, and show that the effects of these types of structures are dealt with effectively by harmonic stripping.

(1) We define a horizontally layered, isotropic model M_0 without a dipping Moho or anisotropy in Table A1. The model, M_d, is the same as M_0 but with Moho tilted by 10° with the up-dip azimuth of 165° relative to North. Synthetic seismograms for every 10° in azimuth are computed (Frederiksen & Bostock 2000), noise is added to the waveform before the time-domain deconvolution is performed to generate Ps receiver functions, $R(\theta, t)$, which are plotted in Fig. A3(a). The dipping Moho creates a sinusoidal variation

to the *P–S* conversions at $\sim$5.5 s in both amplitude and arrival time. Harmonic stripping is applied to the synthetic receiver functions and the resulting estimates A_0, A_1, A_2 are shown in Figs A3(d)–(f). As described by Jones & Phinney (1998), the dipping interface generates a 2π periodicity with the strongest amplitude at the updip azimuth and the arrival time will be delayed most at this azimuth. This phenomenon is observed in the harmonic stripping results. A_1 shows the strongest perturbation at 5–6 s where the *P--S* conversion occurs and A_2 is subtle in this time range. Fig. A3(b) and (c) show the harmonic fit, $H(\theta, t)$, and the difference between H and R, respectively. The random noise added to the seismograms is not mapped into the A_1 or A_2 estimates, but resides exclusively in the residuals, which we take as the uncertainty of the final azimuthally independent receiver function. For comparison, the receiver functions computed from the horizontally layered model M_0 (blue waveform) and the estimate of A_0 (red dashed line) are shown in Fig. A7(a). The arrival times of the *P–S* conversion from both are similar, but the A_0 component recovered from the dipping model (red dashed line) displays a somewhat smaller amplitude because the harmonic stripping method does not fully reproduce the sinusoidal variation in arrival time of the input model (blue line). This inaccuracy, however, is encompassed by the enlargement of the uncertainties near the *P–S* conversion time as discussed further in Section 8.2.

(2) We also test an azimuthally anisotropic model, M_{ani}, in which a 4 per cent azimuthally anisotropic layer between 15 and 45 km depth range with a fast direction at 75° to North is added to M_0. The resulting synthetic receiver functions contaminated by random noise and the results of harmonic stripping are shown in Fig. A4. Azimuthal anisotropy introduces a π periodicity into the arrival
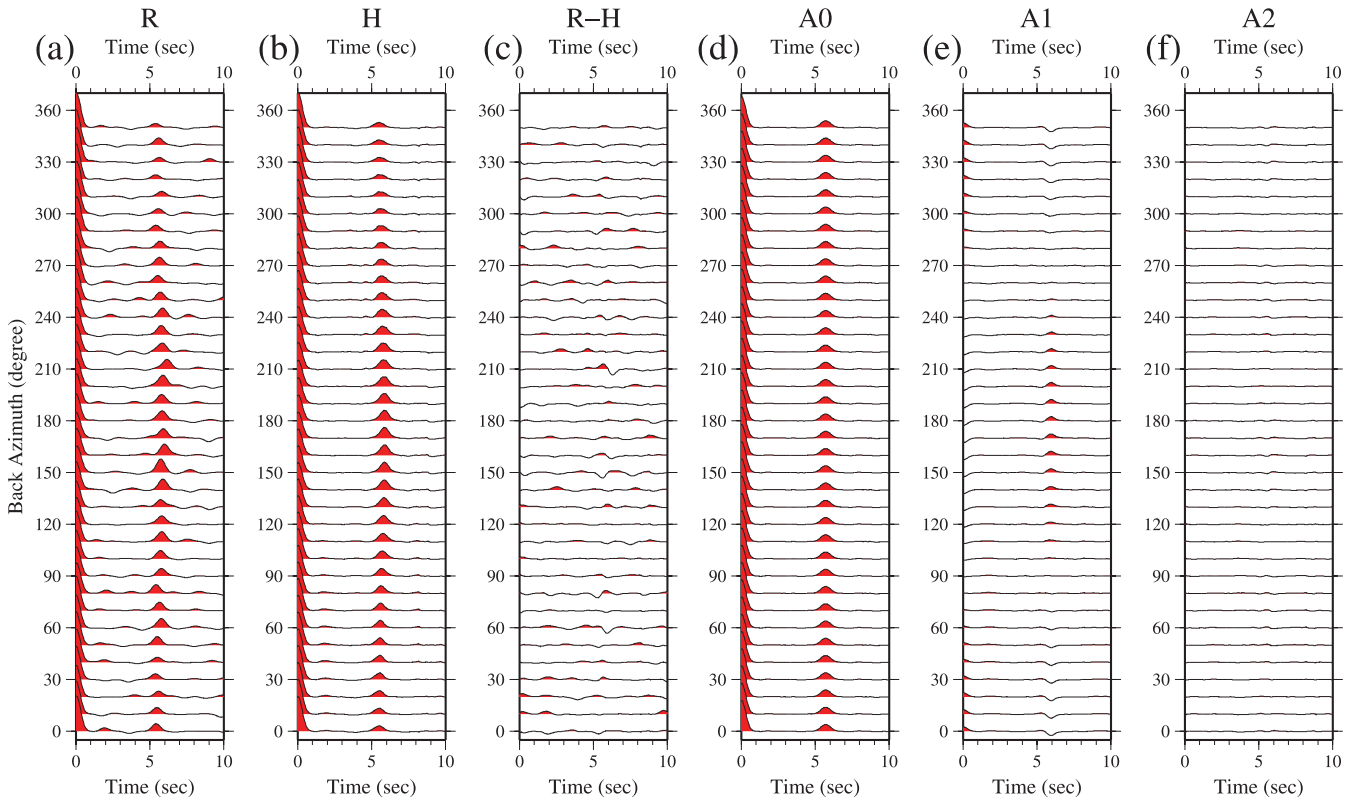

Figure A3. Synthetic experiment performed with Moho dipping 10° with an up-dip azimuth of 165° clockwise from North. (a) The synthetic receiver functions $R(\theta, t)$ including additive noise plotted at the appropriate backazimuth. (b) The estimated receiver functions from harmonic stripping $H(\theta, t)$. (c) The difference between (a) and (b). (d and e) The estimated A_0, A_1, A_2 components from harmonic stripping, respectively.
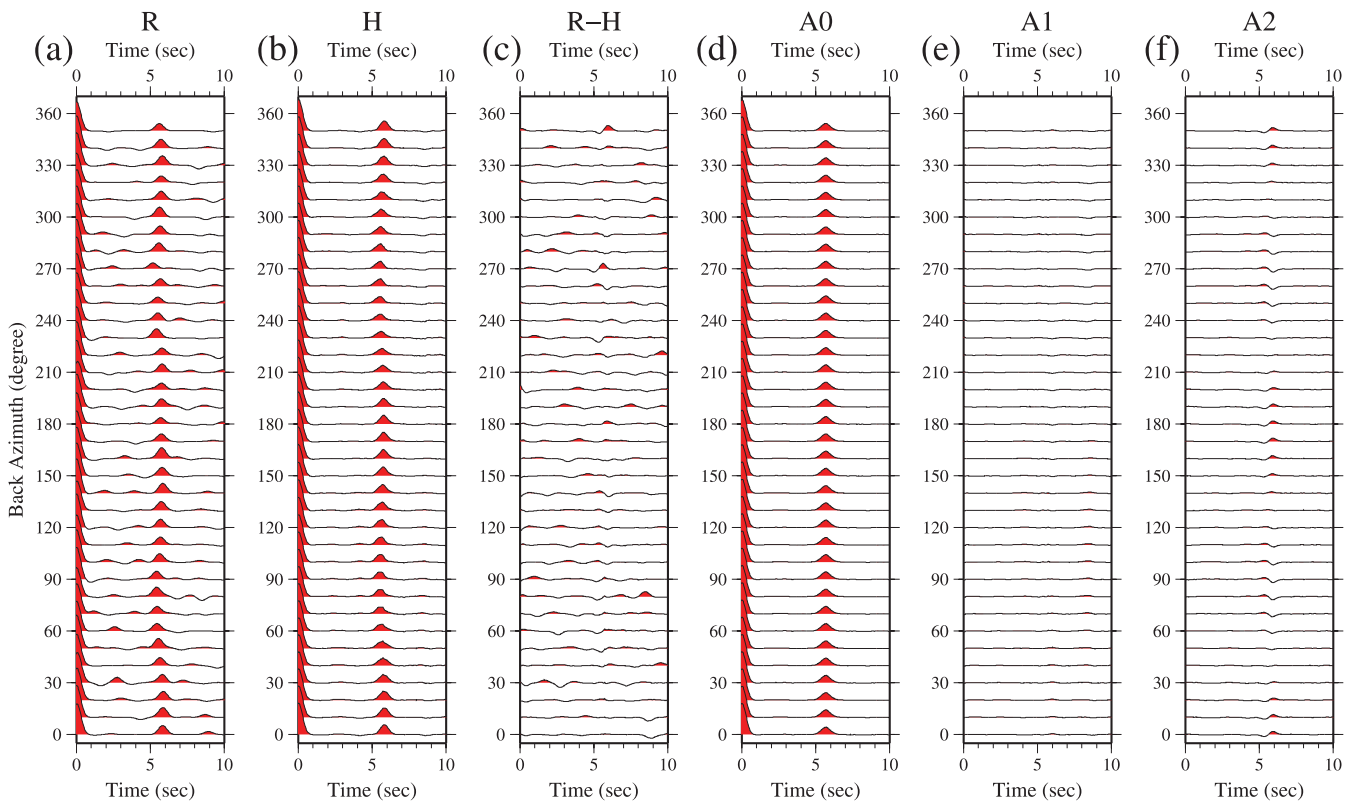
Figure A4. The same as Fig. A3, but for synthetic receiver functions computed from a model with 4 per cent azimuthal anisotropy in the mid-to-lower crust with a fast-axis direction at 75° clockwise from North.
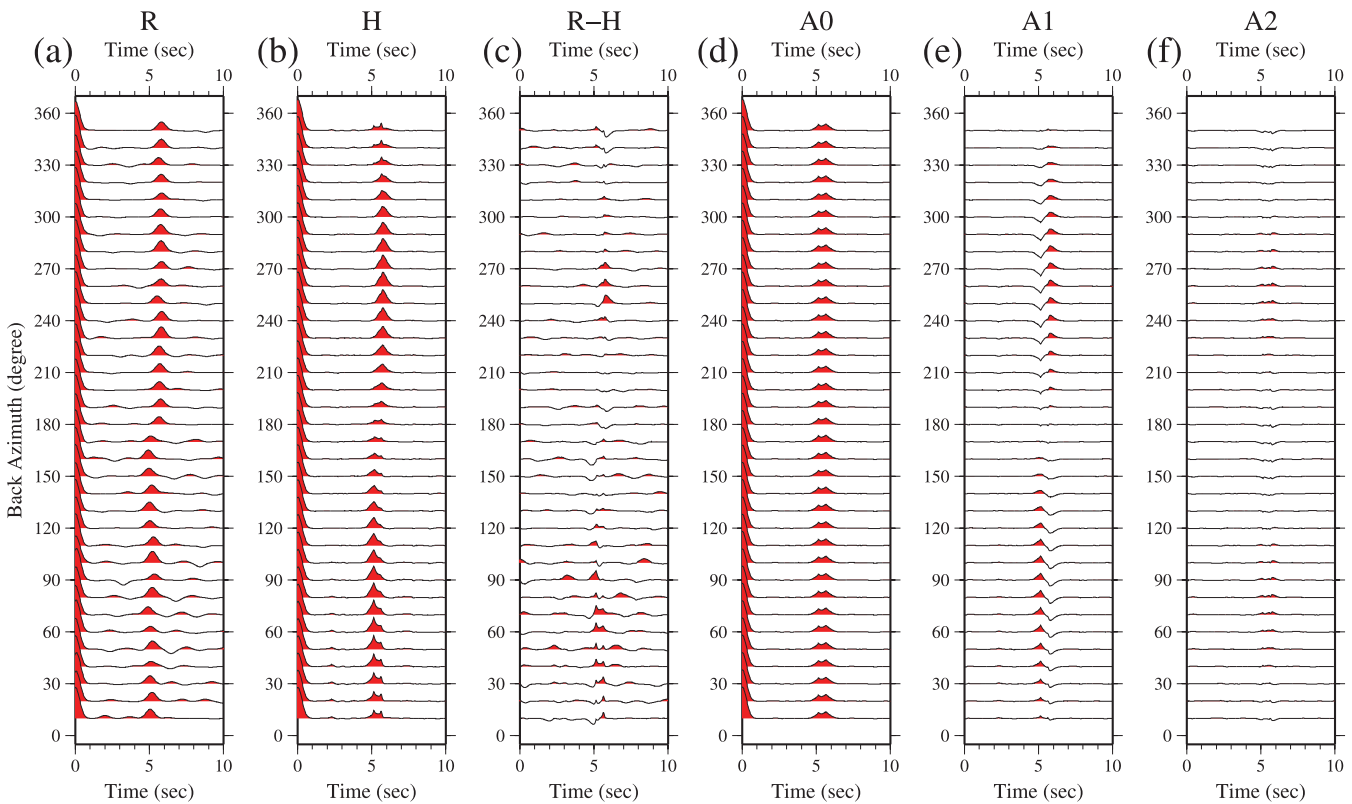

Figure A5. The same as Fig. A3, but for synthetic receiver functions from a model with a 5 km step of crustal thickness such that Moho is at 40 km depth east of the station and 45 km depth west of the station.
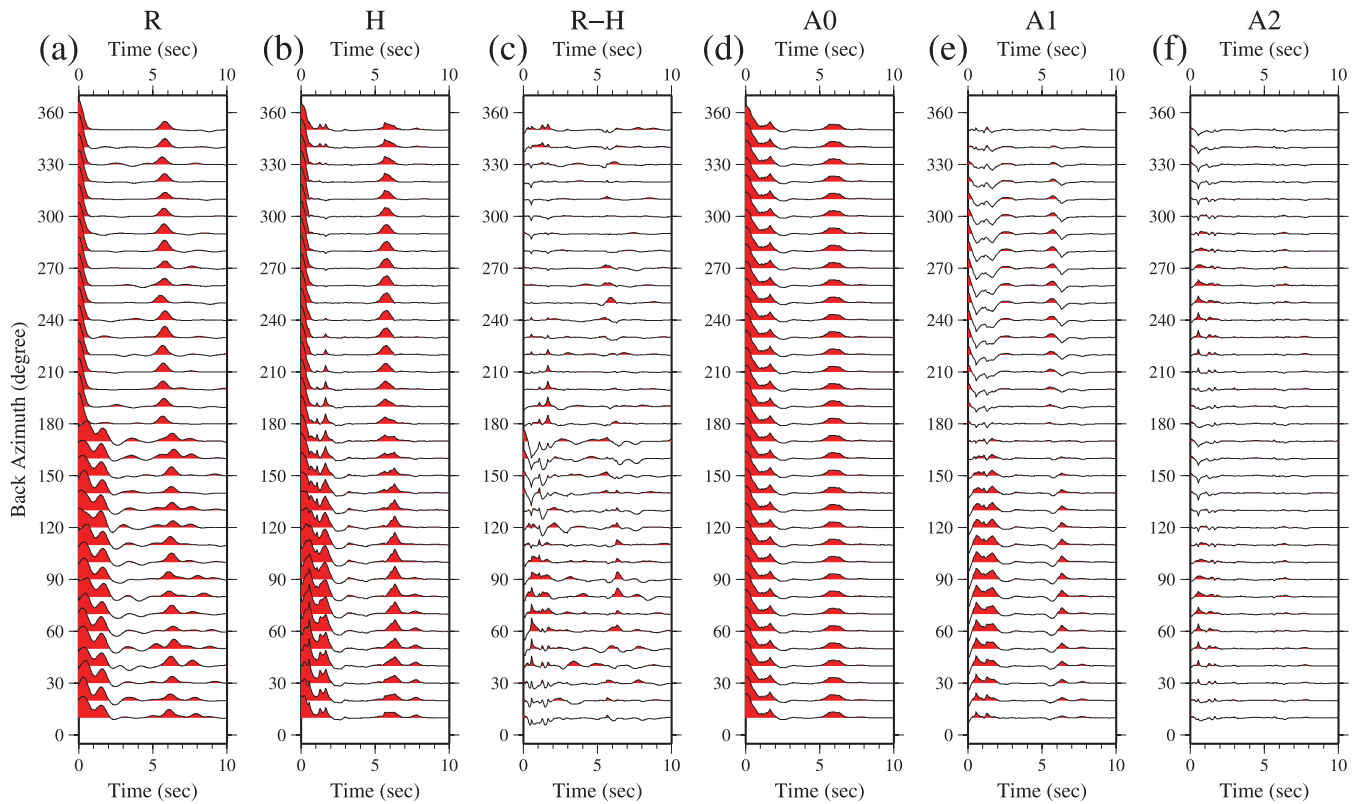
Figure A6. The same as Fig. A3, but for synthetic receiver functions from a model with a 2 km jump of sedimentary layer thickness such that there are no sediments east of the station and 2 km of sediments west of the station.
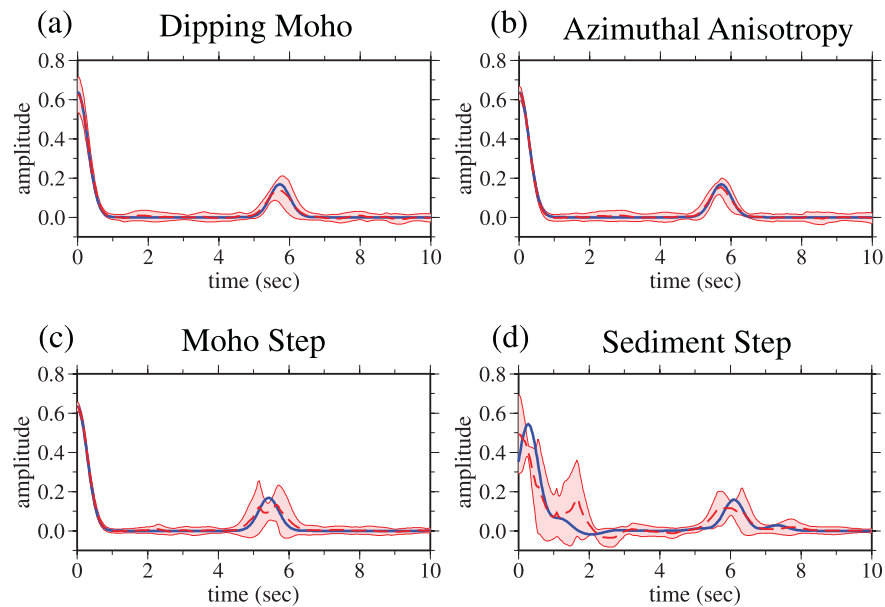

Figure A7. (a) The azimuthally independent A_0 receiver function estimated from harmonic stripping computed from a model with the dipping Moho is shown with the red dashed line. For comparison, the receiver function from the azimuthally averaged model (horizontal Moho) is shown with the blue line. Uncertainties $s(t)$ are outlined by red lines with a light-red fill. (b) The same as (a), but for the A_0 receiver function estimated from synthetic receiver functions computed using a model with 4 per cent anisotropy in the mid-to-lower crust. (c) The same as (a), but for the A_0 receiver function estimated from a model with a step in Moho depth of 5 km at the station. (d) The same as (a), but for a model with a 2 km step in sediment thickness at the station.

times of the *P–S* conversions (Fig. A4a), which appears in the estimated A_2 component (Fig. A4f). The estimated A_0 component is shown in Fig. A7(b) to agree with the receiver function computed from model M_0.

From these tests for structures that vary smoothly with azimuth, a dipping Moho or azimuthal anisotropy in the crust, we conclude that the harmonic stripping technique effectively retrieves the az-imuthally independent component which is an accurate estimate of

the receiver function for an effective horizontally layered, isotropic medium.

Secondly, we test another type of model that possesses azimuthally discontinuous features: (3) a jump in Moho with azimuth and (4) a jump in sediment thickness with azimuth. We show that for azimuthally discontinuous structures, harmonic stripping does not reliably estimate the horizontally layered, isotropic effective medium. The method identifies this problem, however, by enlarging the uncertainties in the time band in which the estimated receiver function diverges from the receiver function of the effective medium.

(3) On the west side of the receiver (backazimuthal angle between 180° and 360°) the model is the isotropic horizontally layered model M_0 with a Moho depth of 45 km, but on the east side Moho is 5 km shallower. Synthetic receiver functions from this model with additive noise are plotted in Fig. A5(a), and the harmonic stripping results are shown in Figs A5(d) and (f). The variations of the receiver functions with backazimuth are not sinusoidal; thus harmonic stripping cannot fit them fully. As a result, the estimated A_0 com-

ponent deviates from the receiver function of the average model (a model with a Moho depth of 42.5 km), which is shown as the blue waveform in Fig. A7(c). However, uncertainties in the A_0 component grow in the time window where A_0 differs from the receiver function of the average model. Thus, in this time band the receiver function will be down-weighted relative to surface wave data, as desired.

(4) Finally, we test of the model with a step in sediment thickness (Fig. A6). The model has a 2 km sedimentary layer west of the receiver and no sediments on its east side. Both models have the same Moho depth. The average model, therefore, has 1 km of sediments. The synthetic receiver functions in Fig. A6(a) display a dichotomous pattern such that the Moho $P–S$ conversion arrival times jumps near 180° azimuth. The estimated A_0 component of the receiver function (Fig. A7d) shows an erroneous double Moho conversion peak as well as relatively large uncertainties that reduce the weight of the receiver function relative to surface wave data in the inversion.